AGU PUBLICATIONS

JGR

Journal of Geophysical Research: Atmospheres

RESEARCH ARTICLE
10.1002/2015JD024623

Special Section:
Deep Convective Clouds and Chemistry 2012 Studies (DC3)

Wet scavenging of soluble gases in DC3 deep convective storms using WRF-Chem simulations and aircraft observations

Megan M. Bela[1,2], Mary C. Barth[3], Owen B. Toon[1,2], Alan Fried[4], Cameron R. Homeyer[5], Hugh Morrison[3], Kristin A. Cummings[6], Yunyao Li[6], Kenneth E. Pickering[6,7], Dale J. Allen[6], Qing Yang[8], Paul O. Wennberg[9,10], John D. Crounse[9], Jason M. St. Clair[7,9,11], Alex P. Teng[9], Daniel O'Sullivan[12], L. Gregory Huey[13], Dexian Chen[13], Xiaoxi Liu[13], Donald R. Blake[14], Nicola J. Blake[14], Eric C. Apel[3], Rebecca S. Hornbrook[3], Frank Flocke[3], Teresa Campos[3], and Glenn Diskin[15]

[1]Department of Atmospheric and Oceanic Sciences, University of Colorado Boulder, Boulder, Colorado, USA, [2]Laboratory for Atmospheric and Space Physics, University of Colorado Boulder, Boulder, Colorado, USA, [3]National Center for Atmospheric Research, Boulder, Colorado, USA, [4]Institute of Arctic and Alpine Research, University of Colorado Boulder, Boulder, Colorado, USA, [5]School of Meteorology, University of Oklahoma, Norman, Oklahoma, USA, [6]Department of Atmospheric and Oceanic Science, University of Maryland, College Park, Maryland, USA, [7]National Aeronautics and Space Administration/Goddard Space Flight Center, Greenbelt, Maryland, USA, [8]Pacific Northwest National Laboratory, Richland, Washington, USA, [9]Division of Geological and Planetary Sciences, California Institute of Technology, Pasadena, California, USA, [10]Division of Engineering and Applied Science, California Institute of Technology, Pasadena, California, USA, [11]Joint Center for Earth Systems Technology, University of Maryland, Baltimore County, Baltimore, Maryland, USA, [12]U.S. Naval Academy, Annapolis, Maryland, USA, [13]School of Earth and Atmospheric Sciences, Georgia Institute of Technology, Atlanta, Georgia, USA, [14]Department of Chemistry, University of California, Irvine, California, USA, [15]NASA Langley Research Center, Hampton, Virginia, USA

Key Points:
- Observed deep convective scavenging efficiencies simulated by simple scheme
- Simulated scavenging efficiencies highly sensitive to ice retention fraction
- Scavenging efficiencies vary among storms with different microphysics

Supporting Information:
- Figure S1
- Figure S2
- Figure S3
- Figure S4
- Figure S5
- Figure S6
- Figure S7
- Figure S8
- Supporting Information S1

Correspondence to:
M. M. Bela,
megan.bela@colorado.edu

Citation:
Bela, M. M., et al. (2016), Wet scavenging of soluble gases in DC3 deep convective storms using WRF-Chem simulations and aircraft observations, *J. Geophys. Res. Atmos.*, *121*, 4233–4257, doi:10.1002/2015JD024623.

Received 8 DEC 2015
Accepted 26 MAR 2016
Accepted article online 2 APR 2016
Published online 21 APR 2016

Abstract We examine wet scavenging of soluble trace gases in storms observed during the Deep Convective Clouds and Chemistry (DC3) field campaign. We conduct high-resolution simulations with the Weather Research and Forecasting model with Chemistry (WRF-Chem) of a severe storm in Oklahoma. The model represents well the storm location, size, and structure as compared with Next Generation Weather Radar reflectivity, and simulated CO transport is consistent with aircraft observations. Scavenging efficiencies (SEs) between inflow and outflow of soluble species are calculated from aircraft measurements and model simulations. Using a simple wet scavenging scheme, we simulate the SE of each soluble species within the error bars of the observations. The simulated SEs of all species except nitric acid (HNO_3) are highly sensitive to the values specified for the fractions retained in ice when cloud water freezes. To reproduce the observations, we must assume zero ice retention for formaldehyde (CH_2O) and hydrogen peroxide (H_2O_2) and complete retention for methyl hydrogen peroxide (CH_3OOH) and sulfur dioxide (SO_2), likely to compensate for the lack of aqueous chemistry in the model. We then compare scavenging efficiencies among storms that formed in Alabama and northeast Colorado and the Oklahoma storm. Significant differences in SEs are seen among storms and species. More scavenging of HNO_3 and less removal of CH_3OOH are seen in storms with higher maximum flash rates, an indication of more graupel mass. Graupel is associated with mixed-phase scavenging and lightning production of nitrogen oxides (NO_x), processes that may explain the observed differences in HNO_3 and CH_3OOH scavenging.

1. Introduction

Deep convective storms produce and transport precursors to ozone (O_3) and aerosols to the upper troposphere (UT), the region within 3–5 km of the tropopause, where they affect climate by modifying the radiative forcing [*IPCC*, 2001]. Furthermore, O_3 in the UT can be transported thousands of kilometers by high-level winds and subsequently brought to the surface by convective downdrafts [*Betts et al.*, 2002], impacting downwind air quality. Measurements from several field campaigns have demonstrated that convection alters the chemistry of the troposphere, including the UT, in regions ranging from the Central U.S.

[*Dickerson et al.*, 1987; *Cooper et al.*, 2006; *Bertram et al.*, 2007; *Hudman et al.*, 2007; *Snow et al.*, 2007; *Fried et al.*, 2008] to central western Europe and the northwestern Mediterranean [*Stickler et al.*, 2006] to West Africa [*Borbon et al.*, 2012].

The amount of O_3 and aerosol formed in the UT depends on the net convective transport of gases that are soluble and reactive in the aqueous and/or ice phase. O_3 formation requires nitrogen oxides (NO_x, the sum of nitric oxide (NO) and nitrogen dioxide (NO_2)) and hydrogen oxides (HO_x, the sum of hydroxyl (HO) and hydroperoxy (HO_2) radicals) [*Jaeglé et al.*, 1998]. However, due to the short lifetime of HO_x, its abundance in the UT is controlled by the net transport of longer-lived HO_x precursors, including hydrogen peroxide (H_2O_2), methyl hydroperoxide (CH_3OOH), and formaldehyde (CH_2O) [*Chatfield and Crutzen*, 1984; *Prather and Jacob*, 1997]. The amount of NO_x in the UT is also affected by the convective transport of the reservoir species nitric acid (HNO_3) [*Grassian*, 2005]. Finally, sulfur dioxide (SO_2) transported by deep convection is thought to be an important source of sulfate aerosol in the UT [*Pruppacher and Klett*, 1997].

A number of chemical and physical processes within the convective core and anvil affect the net transport of soluble species by deep convective clouds, including dissolution in cloud water or liquid phase precipitation [*Seinfeld and Pandis*, 2006], aqueous chemistry [*Barth et al.*, 2007a], and ice deposition of HNO_3 [e.g., *Zondlo et al.*, 1997; *Voigt et al.*, 2006] and H_2O_2 [e.g., *Iribarne and Pyshnov*, 1990]. Deep convective clouds redistribute soluble species when hydrometeors evaporate or freeze and release part of the dissolved gases (partial ice retention) or precipitation reaches the surface (wet deposition). Hydrometeors are liquid water or ice particles in the atmosphere and include cloud droplets, ice particles, rain, snow, graupel, and hail. Collectively, these processes are referred to as wet removal/scavenging. Uncertainties remain in scavenging efficiencies, the fractions of soluble gases in inflow that are removed by storms. Analyses of aircraft observations have calculated scavenging efficiencies ranging from 4–81% for CH_2O [*Borbon et al.*, 2012; A. Fried et al., Convective transport and scavenging of formaldehyde to the upper troposphere and lower stratosphere in thunderstorms over the Central United States during the 2012 DC3 study, *Journal of Geophysical Research Atmospheres*, under review, 2016] to 0–84% for CH_3OOH and 55–97% for H_2O_2 [*Cohan et al.*, 1999; *Barth et al.*, 2016].

A primary source of this uncertainty is the fraction of gases that are retained in ice during hydrometeor freezing. Simulations of an idealized thunderstorm by several cloud-resolving models yielded varying results for CH_2O, H_2O_2, and HNO_3 in convective outflow due to differing microphysics and assumptions about ice retention [*Barth et al.*, 2007b]. Sensitivity simulations of the same storm with a 3-D thunderstorm model showed that when species are completely degassed, they are transported to the UT, while those retained in frozen hydrometeors are removed from the UT by snow and hail [*Barth et al.*, 2001, 2007a]. Observed retention fractions are highly variable. For example, laboratory estimates of the retention fraction for H_2O_2 range from 0.05 to 1.0 [*Iribarne and Pyshnov*, 1990; *Snider et al.*, 1992; *Snider and Huang*, 1998]. Nevertheless, since highly soluble (acidic) gases nearly completely dissociate in the liquid phase, they tend to be more highly retained than less soluble species. For example, HNO_3 (H_{eff} approximately $10^{12} M$ atm^{-1}) has been found to be completely retained [*Iribarne and Pyshnov*, 1990; *von Blohn et al.*, 2011], while a value of 0.02 has been observed for SO_2 (H_{eff} approximately 3400 M atm^{-1}). Nevertheless, a theoretical study showed that in addition to the effective Henry's law coefficient, the retention fraction is related to environmental conditions such as droplet pH, size, temperature, and the air speed around the drop [*Stuart and Jacobson*, 2004].

The ability of atmospheric chemistry-meteorology models to predict the effect of deep convection on UT composition depends on their representation of mass transfer between the gas and aqueous phase, aqueous chemistry, and cloud microphysics. Most models (CMAQ, GEOS-Chem, and WRF-Chem) assume that the dissolved species concentration in the cloud droplets is in Henry's law equilibrium, which may be reached quickly (i.e., within one model time step) for low- and moderate-solubility species. However, for high-solubility species (such as HNO_3), equilibrium may not be reached within a model time step [*Schwartz*, 1986]; thus, a kinetic approach, where mass transfer is parameterized by coefficients for diffusion through the gas phase and across the gas-liquid interface, may produce more realistic results [e.g., in WRF-AqChem [*Barth et al.*, 2001]). While some models (e.g., CMAQ and WRF-Chem using the Carbon Bond Mechanism version Z (CBMZ) mechanism) only calculate scavenging by rain, those that include ice retention and deposition (e.g., GEOS-Chem and WRF-Chem using the Model for Ozone and Related chemical Tracers (MOZART) mechanism) introduce additional parameters that must be estimated [*Barth et al.*, 2007b]. Aqueous chemistry mechanisms

range from simple parameterizations of sulfur chemistry (e.g., in CMAQ [*Walcek and Taylor*, 1986] and GEOS-Chem [*Martin and Good*, 1991; *Alexander et al.*, 2005, 2009, 2012]), to condensed schemes focusing on sulfur chemistry (e.g., in WRF-AqChem [*Barth et al.*, 2007a]), to more complete schemes including oxygen-hydrogen, chlorine, and carbonyl groups (e.g., in Model for Simulating Aerosol Interactions and Chemistry (MOSAIC) [*Pandis and Seinfeld*, 1989; *Fahey and Pandis*, 2001; *Zaveri et al.*, 2008]). Most of the models (e.g., CMAQ, GEOS-Chem, WRF-AqChem, and MOSAIC) calculate pH from charge balance, so the diagnosed pH may be too acidic if some base cations such as Ca^{2+} are missing in the model and charge balance. The simulated cloud droplet size will also affect the calculated pH. As many aqueous reactions are pH dependent, the resulting amounts of species including SO_2, H_2O_2, and CH_2O can be affected [*Hegg and Larson*, 1990; *Roelofs*, 1993; *Barth*, 2006]. Finally, the ability of models to correctly predict liquid water content varies with the grid resolution and microphysics parameterization [*Zhang et al.*, 2007].

In this study, we examine wet removal and ice retention of gases of a range of solubilities and evaluate the capability of a high-resolution meteorology-chemistry model to represent these complex scavenging processes. We analyze thunderstorm case studies from the National Science Foundation (NSF)/NASA Deep Convective Clouds and Chemistry (DC3) field campaign, which took place in the Central U.S. in May–June 2012. DC3 was the first aircraft campaign in this region of the U.S. to simultaneously sample a large suite of trace gases in deep convective inflow and outflow in conjunction with extensive ground-based lightning and radar observations [*Barth et al.*, 2015]. First, we examine the 29–30 May 2012 severe storm in Oklahoma, utilizing aircraft observations to estimate wet removal. We then conduct high-resolution sensitivity simulations with the Weather Research and Forecasting model with Chemistry (WRF-Chem) [*Grell et al.*, 2005; *Fast et al.*, 2006] in order to constrain the fraction of each species retained in ice when cloud water freezes and compare these results with previous studies of idealized and Colorado deep convective storms. Finally, we compare wet removal in the Alabama and Colorado storm cases with the Oklahoma case and other studies ranging from West Africa to the South Pacific.

This study aims to answer the following questions: How well does a simple wet removal scheme in a regional atmospheric chemistry model represent wet removal of different soluble species, using the Oklahoma 29–30 May multicellular storm system from DC3 as an example? What fractions of different soluble species are retained in ice? How much does wet removal of soluble species vary in deep convective storms with a range of dynamical and chemical characteristics?

2. Data and Methods

2.1. DC3 Case Study Storms and Aircraft Measurements

The DC3 field campaign [*Barth et al.*, 2015], based in Salina, Kansas, USA in May–June 2012, examined how deep convective clouds in the continental midlatitudes impact UT chemical composition through convective transport, lightning NO_x production, wet removal, surface sources, dynamics, and UT chemistry. Four storm case studies were selected from DC3 for this work: (1) a multicellular storm system in Oklahoma on 29–30 May with Lightning Mapping Array (LMA) and multiple mobile radar coverage, (2) a discrete ordinary convective (or "air mass") storm in Alabama on 21 May with LMA and dual-polarimetric radar coverage, (3) a strong convective Colorado storm on 6–7 June with excellent dual-polarimetric radar and LMA coverage, and (4) the southern of two convective storms in NE Colorado/SW Nebraska on 22–23 June. Comparing these four cases yields information about differences among storms with a range of dynamical and chemical characteristics. The NASA DC-8 and the NSF/National Center for Atmospheric Research (NCAR) Gulfstream V (GV), carrying chemistry, aerosol, and cloud physics instrumentation, sampled inflow and outflow of these storms. The instruments used to obtain the observations for the scavenging analysis, as well as the uncertainty parameters of the measurements, are listed in Table 1 for the DC-8 and Table 2 for the GV.

Scavenging efficiencies were calculated from measurements of soluble trace gases. On the DC-8, CH_2O measurements were taken with a Difference Frequency Generation Absorption Spectrometer (DFGAS) midinfrared (IR) spectrometer, which is based on absorption spectroscopy using a mid-IR (3.53 μm) laser source [*Weibring et al.*, 2006, 2007]. On the GV, CH_2O observations were obtained with the Compact Atmospheric Multispecies Spectrometer (CAMS), which is very similar to the DFGAS instrument [*Richter et al.*, 2015]. H_2O_2, CH_3OOH, and HNO_3 were measured on the DC-8 with the time-of-flight (ToF-CIMS) mass filter and tandem quadrupole mass filter (T-CIMS) chemical ionization mass spectrometers (CIMS) utilizing reaction with CF_3O^- [*Huey et al.*, 1996; *Amelynck et al.*, 2000; *Crounse et al.*, 2006; *St. Clair et al.*, 2010]. On the GV, H_2O_2 and CH_3OOH observations were obtained with the Peroxide Chemical Ionization Mass Spectrometer (P-CIMS) using CO_4^- and O_2^- reagent ions,

Table 1. Instruments Aboard the DC-8 Aircraft That Obtained the Observations Used in This Study

			Measurement Uncertainties	
Species	Instrument/Method	LLOD (ppb)	Precision (ppb)	Bias (%)
CH_2O	DFGAS	0.05	0.05	3.9
CH_3OOH	CIT-CIMS	—	0.03	H_2O dependent[a]
H_2O_2	CIT-CIMS	—	0.075	50
HNO_3	CIT-CIMS	—	0.1	50
SO_2	GT-CIMS	0.002	—	15
n-butane	WAS	0.003	0.003	or 5
CO	DACOM	—	2	or 2
O_3	Chemiluminescence	—	0.04	3
H_2O vapor	DLH	—	1000	or 5
Liquid/ice water content (g m^{-3})	2D-S IWC	—	—	—

[a] $[H_2O] < 230$ ppmv: 40%; $[H_2O] > 230$ ppmv: $(-9.1 + 20.8 \log_{10}[H_2O])$%.

and HNO_3 was measured by reaction with SF_6^- using the Georgia Tech Chemical Ionization Mass Spectrometer (GT-CIMS) [*Huey*, 2007]. SO_2 was measured using GT-CIMS [*Kim et al.*, 2007] on both aircraft.

Measurements of *n*-butane, which is an insoluble passive tracer on the timescales of the storms, were used in the calculation of scavenging efficiencies from observations to account for entrainment of air from the free troposphere (FT). On the DC-8, *n*-butane was analyzed from canisters with collection time ranging from 30 s to 2 min, increasing with altitude, using the Whole Air Sampler (WAS) [*Blake et al.*, 2003]. On the GV, observations of *n*-butane were obtained from samples collected for 35 s every 2 min with the Trace Organic Gas Analyzer (TOGA) instrument, which includes a mass spectrometer and gas chromatograph [*Apel et al.*, 2015].

Carbon monoxide (CO) observations were used for evaluating model passive tracer transport, an indication of the amount of dilution/entrainment. Additionally, the ratios of O_3 to CO were used to remove observations with stratospheric influence. On the DC-8, CO measurements were obtained with the Differential Absorption CO Measurement (DACOM), a 4.5 μm tunable diode laser [*Sachse et al.*, 1987]. On the GV, CO was measured with an Aero Laser 5002 vacuum UV resonance fluorescence instrument [*Gerbig et al.*, 1999], which observes CO fluorescence from radiation centered at 151 nm with a 10 nm band pass. O_3 measurements on the DC-8 were taken via NO-induced chemiluminescence [*Ryerson et al.*, 2000], in which excited NO_2 is formed from the reaction of NO and O_3 and measured by photon counting. Observations of O_3 on the GV were obtained with the HAIS Fast O_3 instrument, which is similar to the previous NCAR instrument described in *Ridley and Grahek* [1990] and *Ridley et al.* [1992] and also employs NO-induced chemiluminescence.

Liquid water content (LWC) and ice water content (IWC) measurements were used to classify aircraft observation points as either clear sky or in cloud. On the DC-8, IWC was provided by the SPEC 2D-S (Stereo) Optical Array Cloud Particle Imaging Probe (10 μm to 3 mm), but LWC was not measured. On the GV, LWC was obtained

Table 2. Instruments Aboard the GV Aircraft That Obtained the Observations Used in This Study

			Measurement Uncertainties	
Species	Instrument/Method	LLOD (ppb)	Precision (ppb)	Bias (%)
CH_2O	CAMS	0.02–0.03	0.02–0.03	5
CH_3OOH	P-CIMS	0.035	—	45
H_2O_2	P-CIMS	0.035	—	30
HNO_3	GT-CIMS	0.0396	—	20
SO_2	GT-CIMS	0.0119	—	15
n-butane	TOGA	0.0003	0.002	or 15
CO	UV fluorescence	—	3	3
O_3	chemiluminescence	—	—	5
H_2O vapor	VCSEL	—	1%	5
Liquid water content (g m^{-3})	CDP LWC	—	—	—

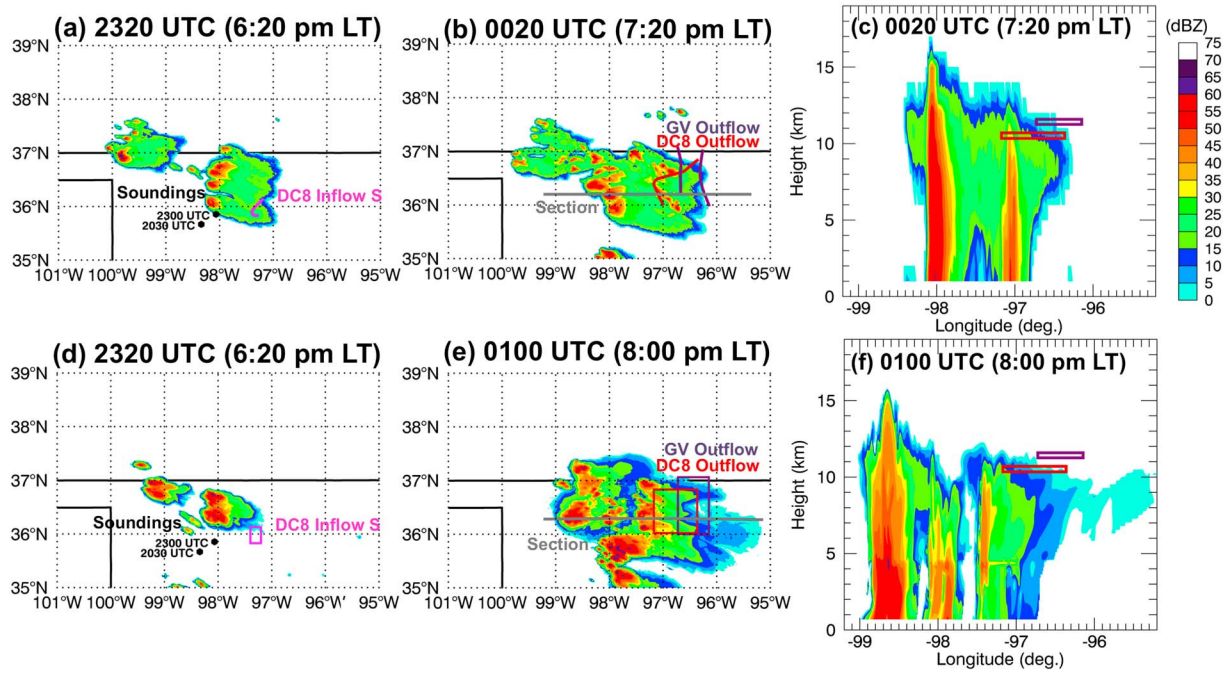

Figure 1. Column-maximum radar reflectivity contours (dB*Z*) from NEXRAD at (a) 2320 UTC on 29 May 2012 and (b) 0020 UTC on 30 May 2012 and (c) east-west vertical reflectivity cross section at the location shown by the gray line in Figure 1b. DC-8 inflow (magenta) and GV (purple) and DC-8 (red) outflow sampling flight segments are shown by lines. Column-maximum radar reflectivity contours (dB*Z*) from WRF-Chem at (d) 2320 UTC on 29 May 2012 and (e) 0100 UTC on 30 May 2012 and (f) east-west vertical reflectivity cross section at the location shown by the gray line in Figure 1e. DC-8 inflow (magenta) and GV (purple) and DC-8 (red) outflow sampling regions are indicated by rectangles. In Figures 1c and 1f, longitudinal and altitude extent of GV (purple) and DC-8 (red) outflow sampling flight segments are designated by rectangles. The NSSL sounding locations are depicted in Figures 1a and 1d.

with the Cloud Droplet Probe (CDP), which determines droplet number and size distributions in the 2.0–50 μm range by shining a laser light on the cloud droplets and measuring the forward scattering [*Lance et al.*, 2010]. IWC was determined with the 2DC Hydrometeor Imaging Probe (2DC), which records the shadow cast by the hydrometeor on a 64-element photodiode array [*Korolev et al.*, 2011].

Water vapor observations were included in calculations of air density, which were needed to convert LWC and IWC to mass mixing ratios. On the DC-8, water vapor mixing ratios were obtained with the Diode Laser Hygrometer (DLH), which uses a differential absorption technique to detect H_2O absorption in the strong combination band near 1.4 μm [*Diskin et al.*, 2002]. On the GV, water vapor was measured with the Vertical Cavity Surface Emitting Laser (VCSEL), which detects H_2O absorption at 1853.37 nm (weak band, lower troposphere) and 1854.03 nm (strong band, middle and upper troposphere) [*Zondlo et al.*, 2010].

2.2. Meteorological Data

The meteorological characteristics of the simulated Oklahoma 29–30 May storm were compared with radar, radio sounding, and precipitation data in order to evaluate the model capability to represent storm dynamics and transport.

Radar observations are from the Next Generation Weather Radar (NEXRAD) program Weather Surveillance Radar-1988 Doppler (WSR-88D) network in the contiguous United States [*Crum and Alberty*, 1993]. WSR-88Ds are S-band (10 cm wavelength) Doppler radars operated by the U.S. National Weather Service. We use methods outlined in *Homeyer* [2014] and updated in *Homeyer and Kumjian* [2015] to create three-dimensional composites of the radar data every 5 min at a horizontal grid spacing of 0.02° latitude and longitude (approximately 2 km) and a vertical grid spacing of 1 km.

The radio sounding data for the Oklahoma 29–30 May storm vicinity were obtained from the National Severe Storms Laboratory (NSSL) Mobile GPS Advanced Upper-Air Sounding System (MGAUS) at 20:29:07 UTC (98.341°W, 35.667°N) and 22:55:59 UTC (98.066°W, 35.854°N) on 29 May 2012. The locations of the two NSSL radio soundings relative to the observed and simulated storm locations, as well as the NEXRAD and WRF-Chem maximum reflectivities at the end of the inflow sampling period, are depicted in Figures 1a and 1d,

respectively. The NSSL system moved its location between the sounding times. Hourly precipitation data were provided by the National Centers for Environmental Prediction (NCEP) Stage IV analysis, a 4 km CONUS grid mosaic of radar and gauge analyses from the regional River Forecast Centers.

2.3. Oklahoma 29–30 May Storm Simulation Setup and Model Description

Simulations of the Oklahoma 29–30 May multicellular storm system were conducted with WRF-Chem V3.6.1. A 1 km horizontal grid spacing domain covering the storm region (southwest corner: 33.82°N, 99.89°W; northeast corner: 38.15°N, 95.11°W) was used. The grid domain is depicted in the supporting information. There were 89 vertical levels, with grid spacing ranging from 50 m in the first model level above the ground to 150–200 m in the upper part of the boundary layer and 250 m in the upper troposphere. The model top was located at 50 hPa (20.6 km). The simulations were initialized on 29 May 2012 at 18 UTC, and meteorological initial and boundary conditions were obtained from the North American Mesoscale Analysis (NAM-ANL) with a 6-hourly time resolution and 12 km horizontal grid spacing. Chemical and initial boundary conditions were obtained from DC-8 profiles in the boundary layer and free troposphere and from the Model for Ozone and Related chemical Tracers, version 4 (MOZART-4) global chemistry model [*Emmons et al.*, 2010] with a 1.9° × 2.5° horizontal grid spacing. Full details on the generation of the chemical initial and boundary conditions and the trace gas profiles are found in the supporting information.

Assimilation of 10 min Earth Networks Total Lightning Network (ENTLN) lightning flash counts [*Fierro et al.*, 2012] was applied from 18 to 21 UTC to attain a more realistic storm evolution. The assimilation scheme adds water vapor between the 0°C and −20°C isotherms, in grid points where the relative humidity is less than 81% according to the following equation:

$$Q_v = AQ_{\text{sat}} + BQ_{\text{sat}} \tan h(CX)\left[1 - \tan h\left(DQ_g^{\alpha}\right)\right] \quad (1)$$

where Q_v, Q_{sat}, and Q_g are the water vapor mixing ratio, saturation water vapor mixing ratio, and graupel mixing ratio (g kg^{-1}), respectively; X is the total flash rate ([10 min]$^{-1}$), and $\alpha = 0.22$, $A = 0.81$, $B = 0.2$, $C = 0.01$, and $D = 0.25$ are constants [*Fierro et al.*, 2012].

The model physics and chemistry options that were used are summarized in Table 3. Cloud microphysical simulations were calculated with the Morrison two-moment scheme [*Morrison et al.*, 2009]. The Yonsei University (YSU [*Hong et al.*, 2006]) Planetary Boundary Layer (PBL) and Noah land surface [*Koren et al.*, 1999] parameterizations were utilized. Land use was provided by a global 1 km vegetation data set derived from observations from the Moderate Resolution Imaging Spectroradiometer (MODIS).

The results presented here are from the simulation most similar to observations based on storm timing, area of high reflectivity, size as observed by NEXRAD, and inflow and outflow aircraft gas measurements. Many alternative grid configurations, horizontal and vertical grid spacings, meteorology and chemistry initializations, and physics options were tested. These alternatives included the North American Mesoscale (NAM) and the North American Regional Reanalysis initializations at 12 UTC and the Data Assimilation Research Testbed forecasts from the campaign initialized at 12 UTC and 18 UTC, the Thompson and NSSL microphysics schemes, and the Mellor-Yamada-Janjic (MYJ) and Mellor-Yamada-Nakanishi-Niino (MYNN) PBL schemes. These results are not shown here, but the sensitivity of simulated vertical transport of soluble species to grid configurations and physical parameterizations could be assessed in a future study.

The Rapid Radiative Transfer Model for GCMs (RRTMG) radiation [*Iacono et al.*, 2008] and Tropospheric Ultraviolet and Visible (TUV) photolysis schemes [*Madronich*, 1987] were used. Gas phase chemistry was represented with the MOZART mechanism [*Emmons et al.*, 2010]. The Goddard Chemistry Aerosol Radiation and Transport (GOCART [*Chin et al.*, 2002]) aerosol scheme was utilized with aerosol direct radiative effects (no aerosol indirect radiative effects were included). Fire emissions were generated from the Fire INventory of NCAR (FINN) [*Wiedinmyer et al.*, 2011], based on MODIS fire count data with 1 km horizontal grid spacing, and plume rise was calculated online every 30 min. Anthropogenic emissions came from the 2011 National Emissions Inventory (NEI). Biogenic emissions were calculated online by the Model of Emissions of Gases and Aerosols from Nature v2.04 (MEGAN [*Guenther et al.*, 2006]).

The representation of production of NO_x by lightning is the same method that was used by *Barth et al.* [2012]. To predict flash rates, the *Price and Rind* [1992] flash rate parameterization scheme was used, which determines the total flash rate from maximum vertical velocity. In this study, the w_{max} scheme was used,

Table 3. WRF-Chem Model Configuration and Physics and Chemistry Options[a]

Simulation Time	2012-5-29 18 UTC to 2012-5-30 02 UTC
Initial/Boundary Conditions	Meteorology: NAM ANL 18 UTC (12 km, 6-hourly) Chemistry (constant BCs, IC reset at 21 UTC): median DC-8 profile (inflow 2310–2317 UTC, free trop 2049–2107 UTC), mean of MOZART at 21 UTC above
Lightning Data Assimilation	18–21 UTC (ENTLN [*Fierro et al.*, 2012])
Grid resolution	$dx = dy = 1$ km, $dz = 50–250$ m
nx, *ny*, *nz*	$420 \times 480 \times 89$
Time step	3 s
Cloud microphysics	Morrison
Deep/shallow convection	explicitly represented
Planetary boundary layer	YSU
Land surface	Noah
Short/longwave radiation	RRTMG
Photolysis	F-TUV
Trace gas chemistry	MOZART
Aerosol scheme	GOCART
Wet deposition	Neu and Prather
Anthropogenic emissions	NEI 2011
Biogenic emissions	MEGAN v2.04
Biomass burning emissions	FINN
Lightning flash rate	w_{max} [*Price and Rind*, 1992], total flashrate multipled by 0.106, distributed within 20 dB*Z*, IC:CG ratio from *Boccippio et al.* [2001], IC/CG vertical distributions from *DeCaria et al.* [2005]

[a] Acronyms are explained in text.

which calculates the flash rate based on the maximum vertical velocity in each processor tile (20×20 horizontal grid points). Flashes were distributed horizontally within the region with reflectivity greater than 20 dB*Z* [*DeCaria et al.*, 2005]. Since the w_{max} scheme overestimates the total flash rate for the storm by a factor of 10 relative to NLDN observations (cloud-to-ground (CG) flashes scaled up to total flashes using *Boccippio et al.* [2001] ratios of intracloud (IC) to CG flashes), a flash rate adjustment factor of 0.106 was applied within the model in order to simulate the correct total number of flashes [*Cummings*, 2015; K. A. Cummings et al., Lightning NO_x production, transport and chemistry in WRF-Chem simulations of Oklahoma, Colorado and Alabama thunderstorms observed during DC3, *Journal of Geophysical Research Atmospheres*, in preparation, 2016a]. The ratio of IC to CG flashes is then estimated from the climatology of *Boccippio et al.* [2001], using values from a $0.5° \times 0.5°$ grid with 3.5° spatial smoothing, and the flashes are distributed vertically according to the IC and CG vertical distributions given in *DeCaria et al.* [2005]. The number of IC and CG flashes in each grid cell is then multiplied by a fixed number of moles of NO produced per IC and CG flash. In these simulations, values of 125 mol NO per IC and CG flash were used as they provided good agreement with NO_x observations in the storm anvil (results are shown in the supporting information). A complete evaluation of lightning NO_x production in the WRF-Chem Oklahoma 29–30 May simulation is given in K. A. Cummings et al. (Application of new and previously developed flash rate parameterization schemes in a cloud-resolved WRF simulation of the 29 May 2012 Oklahoma thunderstorm observed during DC3, *Journal of Geophysical Research Atmospheres*, in preparation, 2016b).

The wet removal scheme in WRF-Chem for MOZART chemistry, based on *Neu and Prather* [2012] (denoted NP2012), was used to compute the dissolution of soluble gases into precipitation and their release into the gas phase upon evaporation of hydrometeors. NP2012 estimates trace gas removal by multiplying the effective Henry's law equilibrium aqueous concentration by the net precipitation formation (conversion of cloud water to precipitation, minus evaporation of precipitation). Additionally, for species with ice deposition

Table 4. Ice Retention Fraction Values for Each Soluble Species WRF-Chem Simulation

	CH_2O	CH_3OOH	H_2O_2	HNO_3	SO_2
no scav.	0	0	0	0	0
scav. R0	0	0	0	0	0
scav. R0.25	0.25	0.25	0.25	0.25	0.25
scav. R0.5	0.5	0.5	0.5	0.5	0.5
scav. R1	1	1	1	1	1
scav. Rvar	0.64	0.02	0.64	1	0.02

(in these simulations, HNO_3), a constant fraction (r_f, retention factor) of 0.5 of the amount soluble prior to freezing of each species is returned to the gas phase for mixed-phase conditions (258 K $< T <$ 273 K). Details of the NP2012 mass transfer calculations are found in the supporting information. The NP2012 scavenging scheme also represents the deposition of HNO_3 on ice with a burial model in which HNO_3 is deposited together with water vapor and buried [*Kärcher and Basko*, 2004; *Ullerstam and Abbatt*, 2005; *Kärcher and Voigt*, 2006]. For rapidly growing ice crystals, the burial model may be more appropriate than the traditional dissociative Langmuir theory, in which gas phase species adsorb onto the ice surface as a function of their partial pressures [*Abbatt*, 1997; *Tabazadeh et al.*, 1999].

It is important to note that only the gas phase concentrations are predicted, so that information about species in the aqueous and ice phase is not transported among grid cells or retained from one time step to the next. With the small (3 s) time step of the Oklahoma 29–30 May simulations, the lack of tracking of the aqueous phase tends to overestimate wet removal, as dissolved species which would be released to the gas phase when hydrometeors evaporate or freeze in different vertical levels are completely removed in the model. Thus, the model does not compute wet deposition at the surface. Additionally, the WRF-Chem simulations in the present study do not include aqueous chemistry or aerosol scavenging. *Yang et al.* [2015], a similar paper to this study, focus on aerosol wet removal of the same Oklahoma 29–30 May storm.

Since there is observational evidence that soluble species other than HNO_3 are retained in the ice phase (section 1), sensitivity simulations were conducted with WRF-Chem varying the retention fraction. The simulation without any liquid or ice phase scavenging is labeled no scav., and the five simulations with scavenging, which all remove soluble species in cloud water and rain but assume that different fractions of trace gases are retained when hydrometeors freeze, are named R0 ($r_f = 0$), R0.25 ($r_f = 0.25$), R0.5 ($r_f = 0.5$), R1 ($r_f = 1.0$), and Rvar (r_f = values varying by species, as defined in *Leriche et al.* [2013]). The r_f values for each species and simulation are listed in Table 4.

The simulations were conducted on the NCAR Yellowstone supercomputer [*CISL*, 2012], using 576 processors (36 nodes, 32 GB memory per node). Approximately 28 h of computing time were needed to simulate periods of 7 h.

2.4. Scavenging Efficiency Calculation

Scavenging efficiencies can be calculated in different ways but are designed to quantify the fraction of a soluble species removed by a storm between inflow and outflow. In the present study, for comparing the model and observations, we are interested in the net amount of each species transported from inflow (boundary layer) to outflow (anvil). Using the ratios of the various chemical species to a long-lived hydrocarbon accounts for the amount of dilution of the soluble species due to entrainment of free tropospheric air in the storm core and anvil. The hydrocarbon ratios represent the correct amount of dilution of the soluble species as long as the hydrocarbon has a long lifetime relative to the timescale of the storm, and the hydrocarbon and the soluble species have similarly shaped background profiles. In the present study we use *n*-butane to account for entrainment/dilution. For the storm cases analyzed here, A. Fried et al. (under review, 2016) calculate equivalent CH_2O scavenging efficiencies in nearly all cases using this *n*-butane ratio method and a more complex altitude-dependent entrainment model. The other soluble species analyzed in the present study drop to a small fraction of their PBL mixing ratios in the free troposphere, although mixing ratios of the peroxides in particular do not decline as rapidly above the boundary layer as *n*-butane. The background profiles of *n*-butane, CO, and the soluble species are shown in the supporting information.

Table 5. Inflow and Outflow Periods for Selected DC3 Storm Cases

Storm/Sampling Type	Time (UTC)	Altitude Range (km)	WRF Times (UTC)
OK 29–30 May			
DC-8 inflow S	23:10:21–23:15:53	1.24–1.27	23:10–23:20
DC-8 outflow	23:48:30–23:58:30	10.34–10.70	00:30–00:40
GV outflow	23:59:30–24:23:30	11.25–11.59	00:40–01:00
AL 21 May			
DC-8 inflow	19:30:43–19:38:00	1.18–1.22	
GV outflow	20:50:30–21:14:30	10.04–10.06	
CO 6–7 June			
DC-8 inflow	22:13:40–22:25:12	1.58–1.81	
GV inflow	23:50:30–23:55:30	2.43–2.47	
DC-8 Outflow	23:56:30–00:09:30	11.81–11.92	
GV outflow	22:20:30–22:53:30	10.35–11.59	
CO 22–23 June S S storm			
DC-8 inflow	22:31:27–22:45:54	1.94–1.99	
DC-8 outflow	01:16:30–01:20:30	10.64–10.72	

Observed inflow locations are cloud-free points in the boundary layer along a flight track where the observed wind was directed toward the storm. Inflow in the model was defined as all model grid points falling within the 3-D latitude-longitude-altitude box defined by the aircraft track (Figures 1a and 1d). Passive tracer WRF simulations (not shown) confirmed that the southern inflow region from the surface to 2 km above ground level (the approximate simulated PBL height) was ingested by the simulated storm and contained in model storm outflow.

Outflow measurements were obtained in the anvil cloud. The storm triggers in the model approximately 40 min later than observed, so for each 10 min increment of outflow observation, model output from the same latitude-longitude-altitude box but 40 min later than observations was used, since this time shift provided the best agreement in anvil size and location as observed by NEXRAD and simulated by WRF-Chem.

For inflow, only cloud-free observation and model points were used, while for outflow, only in-cloud gas phase mixing ratios were included. Cloud-free points are defined as $Q_{tot} < 0.01$ g (kg dry air)$^{-1}$, where Q_{tot} is the total liquid and ice mixing ratio, with Q_{tot} in the simulation given by the sum of $Q_{cloudwater}$, Q_{ice}, Q_{rain}, Q_{snow}, and $Q_{graupel}$, and the observed Q_{tot} is provided by either the CDP LWC or the 2DC IWC for the GV and by the 2D-S IWC for the DC-8. Additionally, points with stratospheric influence, defined as $O_3/CO > 1.25$ [*Hudman et al.*, 2007], were removed for both inflow and outflow. The time periods and altitude ranges of inflow and outflow sampling for each aircraft and storm are listed in Table 5. For analysis of the Oklahoma 29–30 May and Colorado 6 June storms, only DC-8 peroxide (H_2O_2 and CH_3OOH) outflow measurements were used in order to be consistent with *Barth et al.* [2016].

From the observations, we define the scavenging efficiency (SE) as

$$\mathrm{SE}(\%) = 100 * \left(1 - \frac{\left(\frac{1}{N}\sum_{i=1}^{N}\frac{S_i}{n\text{-butane}_i}\right)_{\mathrm{outflow}}}{\left(\frac{1}{N}\sum_{i=1}^{N}\frac{S_i}{n\text{-butane}_i}\right)_{\mathrm{inflow}}}\right) \quad (2)$$

where S_i and n-butane$_i$ are the individual observations of gas phase mixing ratios (ppbv) of species S and n-butane, respectively, and N is the number of observations.

Since n-butane is insoluble, the "scavenging efficiency" for n-butane is an indication of the amount of dilution of storm outflow with free tropospheric air that is entrained along the storm core and is calculated as follows:

$$\mathrm{SE}(\%) = 100 * \left(1 - \frac{\left(\frac{1}{N}\sum_{i=1}^{N} n\text{-butane}_i\right)_{\mathrm{outflow}}}{\left(\frac{1}{N}\sum_{i=1}^{N} n\text{-butane}_i\right)_{\mathrm{inflow}}}\right) \quad (3)$$

The MOZART chemical mechanism does not include *n*-butane or a similarly long-lived hydrocarbon. Therefore, we determine the scavenging efficiency in the WRF-Chem simulation by calculating the fractional difference in mean outflow values between each simulation with scavenging from the simulation without scavenging:

$$\mathrm{SE}(\%) = 100 * \left(\frac{q_{i,\mathrm{noscav}} - q_{i,\mathrm{scav}}}{q_{i,\mathrm{noscav}}} \right) \quad (4)$$

where $q_{i,\mathrm{noscav}}$ and $q_{i,\mathrm{scav}}$ are the mean outflow values of species i in the simulation without wet scavenging and a given simulation with wet scavenging, respectively.

3. Oklahoma 29–30 May Storm

The first two objectives of this study are to evaluate the NP2012 wet removal scheme and determine ice retention fractions for the DC3 Oklahoma 29–30 May storm case. Thus, we present background on observations of the Oklahoma 29–30 May case then evaluate the simulations that use different ice retention fractions with observed meteorological parameters and scavenging efficiencies.

3.1. Observations

The Oklahoma 29–30 May storm was chosen as the first case study due to its nearly complete LMA and radar coverage and its isolated and severe storm dynamics that facilitate inflow/outflow analysis. The prestorm atmosphere had relatively high shear (19 m s^{-1}) from 0 to 6 km and high convective available potential energy (CAPE) (3113 J kg^{-1}) at 20 UTC as determined from prestorm soundings, and aircraft observations showed high anthropogenic and moderate biogenic emissions (approximately 50 pptv toluene/260 pptv isoprene in the PBL) [*Barth et al.*, 2015]. The storm initiated at around 21 UTC on 29 May 2012 on the Oklahoma/Kansas border ahead of a cold front and dryline and continued to grow and track to the southeast until about 04 UTC on 30 May 2012. The aircraft sampled the prestorm environment and the storm between 20 UTC on 29 May and 02 UTC on 30 May. The DC-8 sampled both storm inflow and outflow, while the GV focused on outflow. Ground-based measurements of the storm included the Shared Mobile Atmospheric Research and Teaching Radar (SMART-R) and National Severe Storms Laboratory (NSSL) and University of Oklahoma (OU) NO-XP mobile radars, the Oklahoma LMA, NSSL, and DOE-ARM Southern Great Plains environmental soundings, and balloon-borne Electrostatic Force Microscopy and Imager of electrical activity. Observed (NEXRAD composite) column-maximum radar reflectivity at the end of the aircraft outflow measurement period (Figure 1b) shows multiple storm cores arranged along a NW/SE axis. In addition, Figure 1c depicts a vertical cross section from NEXRAD through the southwestern core, which reached an altitude of 17 km with reflectivities of up to 60 dB*Z*. SMART-R radar observations of this southwesternmost cell revealed maximum updraft velocities of 65 m s^{-1} between 8 and 9.5 km above sea level (asl) at 2330 UTC on 29 May 2012 (M. Biggerstaff, personal communication, 2014).

3.2. Comparison of Observations and WRF-Chem Simulations

3.2.1. Meteorology

We now compare meteorological observations and WRF-Chem simulations of the Oklahoma 29–30 May case to evaluate the capability to simulate the observed storm morphology and trace gas transport. Column-maximum radar reflectivity observed with NEXRAD and simulated with WRF-Chem are compared in Figure 1 at two stages of storm development corresponding to the ends of the aircraft inflow and outflow measurement periods. In addition, Figure 1 shows vertical cross sections from NEXRAD and WRF-Chem at the end of the outflow period.

In WRF-Chem, the reflectivity is calculated in the Morrison microphysics scheme using the Rayleigh approximation at a wavelength of 10 cm. The storm location, size, and structure (intensity, anvil height, and extent) are well represented by the model compared to NEXRAD, but the storm triggers in the model approximately 40 min later than observed. Also, at the end of the outflow period, the model arranges the line of cores along a NE/SW axis versus the observed NW/SE orientation. The WRF-Chem simulation exhibits larger core regions of moderate to high reflectivity (40–60 dB*Z*) compared with NEXRAD. This may be due to layers of hail in the model at high levels, rather than to the wider storm-simulated cores than observed, and future analysis will include comparison with hydrometeor distributions derived from the SMART-R radar observations.

Figure 2 depicts radio soundings of temperature, dew point, and wind at 20:29:07 UTC and 22:55:59 UTC and WRF-Chem profiles in the nearest grid points at 2030 UTC and 2340 UTC, respectively. Extracting the second

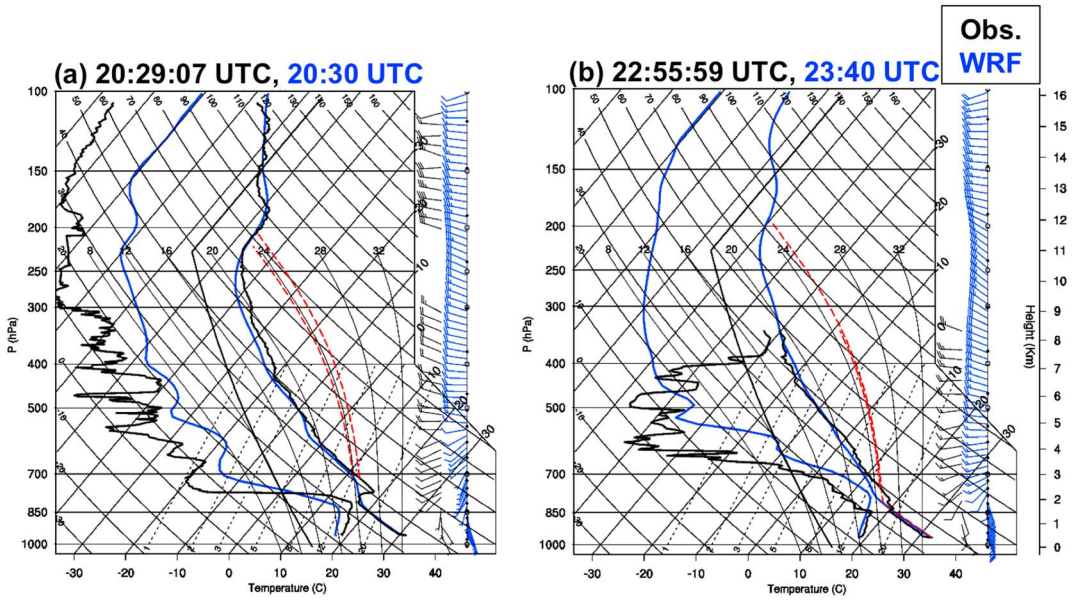

Figure 2. Temperature, dew point, and wind profiles from radio soundings (black) and WRF-Chem (blue) for (a) NSSL MGAUS (98.341°W, 35.667°N) at 20:29:07 UTC and (b) NSSL MGAUS (98.066°W, 35.854°N) at 22:55:59 UTC (obs.) and 23:40 UTC (WRF-Chem) on 29 May 2012. The red dashed lines indicate the regions used to calculate CAPE for observations: 3114 J kg^{-1} in Figure 2a and 1876 J kg^{-1} (no radio sounding information above approximately 320 hPa) in Figure 2b and for WRF-Chem: 2780 J kg^{-1} in Figure 2a and 3290 J kg^{-1} in Figure 2b.

sounding from 40 min later in the model was necessary due to the later triggering of the simulated versus observed storm. Observed potential temperatures below 850 hPa are about 35°C in both soundings, as they are in the simulations. However, dew point temperatures below 870 hPa are about 2°C lower in WRF-Chem than in the sounding (16°C versus 18°C) at 2030 UTC and about 1°C lower in WRF-Chem than observed (17°C versus 18°C) at 2300 UTC. The underestimate of boundary layer moisture in the model may contribute to the delay in storm initiation. Winds are well represented in both direction and magnitude. The model is significantly drier above 400 hPa at 2340 UTC than in the 22:55:59 UTC sounding, but this is likely because the sounding was ingested into the storm at this altitude.

Figure 3 depicts mean hourly precipitation from 2300 to 0000 UTC from the NCEP Stage IV analysis and from 2340 to 0040 UTC from WRF-Chem (rain and graupel). The observations show maximum precipitation rates of up to 56 mm h^{-1} in the storm cores, while WRF-Chem produces a maximum precipitation rate of 34 mm h^{-1} in the cores and wider than observed areas of lower precipitation rates. Despite these differences in the precipitation distribution, the total precipitation volume in the main northeastern storm cluster sampled by the aircraft is similar in the observations and model (obs.: 23–00 UTC - 4.88 × 10^7 m^3, 21–00 UTC - 6.00 × 10^7 m^3; WRF-Chem: 2340–0040 UTC - 5.04 × 10^7 m^3, 2140–0040 UTC - 7.14 × 10^7 m^3). Therefore, the total amount of precipitation for the storm cluster from approximately the time of convective initiation until the end of the

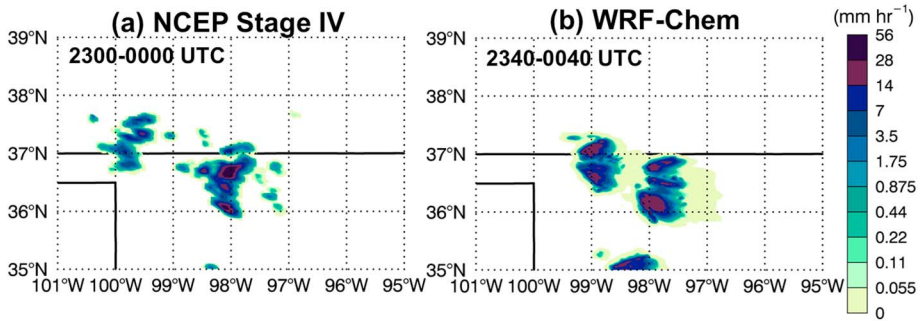

Figure 3. Hourly mean precipitation rate (mm h^{-1}) from (a) 29 May 2012 2300 UTC to 30 May 2012 0000 UTC from the NCEP Stage IV analysis and (b) 29 May 2012 2340 UTC to 30 May 2012 0040 UTC from WRF-Chem.

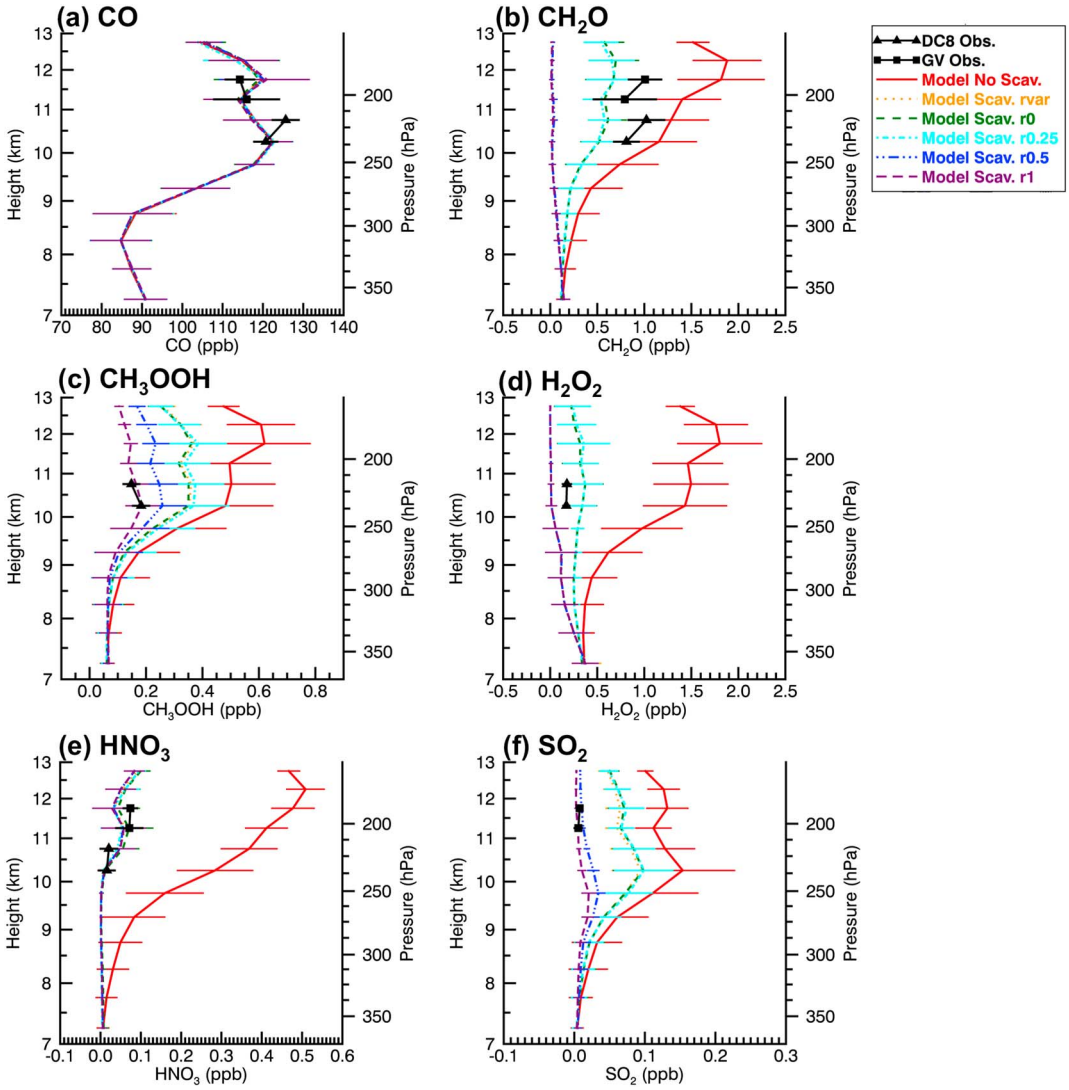

Figure 4. Mean outflow chemical profiles from the Oklahoma 29–30 May 2012 storm as observed by the DC-8 (black triangles and solid lines) and GV (black squares and solid lines) aircraft and mean profiles within the aircraft outflow sampling latitude-longitude region and vertical extent of anvil cloud as simulated by WRF-Chem without (solid red) and with wet removal (Rvar = dot orange; R0 = dash green; R0.25 = dash-dotted cyan; R0.5 = dash dot dot dot blue; and R1 = long dash purple), for (a) CO, (b) CH_2O, (c) CH_3OOH, (d) H_2O_2, (e) HNO_3, and (f) SO_2. The error bars indicate one standard deviation.

DC-8 outflow period/beginning of the GV outflow period (obs.: 2100–0000 UTC; WRF-Chem: 2340–0040 UTC) in the simulations is within 20% of the observations. In a future study, simulated and polarimetric radar retrievals of hydrometeor distributions will be compared in order to determine whether the model has the correct hydrometeor vertical distribution and liquid/ice phase partitioning.

3.2.2. Scavenging Efficiencies

We now compare aircraft observations and WRF-Chem simulations of the Oklahoma 29–30 May case to evaluate the capability of the current wet scavenging scheme to reproduce the observed scavenging efficiencies of soluble species. Figure 1 marks the aircraft flight tracks and corresponding latitude and longitude regions for the WRF-Chem simulations that were designed to sample regions of storm inflow and outflow. Since no DC-8 SO_2 measurements were available on 29 May, observed inflow values were estimated from the mean SO_2 to *n*-butane ratios from the nearby DC-8 boundary layer sampling on flights on 19 and 25 May in Oklahoma (the same flight segments used for the SO_2 model initial and boundary conditions), restricted to the 29–30 May inflow sampling altitude range (1.23–1.32 km).

Table 6. Values From Observations and WRF-Chem Simulations of the Oklahoma 29–30 May Storm of Mean Mixing Ratios (ppb) of CO and Soluble Species in Outflow Regions

	CO (ppb)		CH_2O (ppb)		CH_3OOH (ppb)		H_2O_2 (ppb)		HNO_3 (ppb)		SO_2 (ppb)	
Obs./Simulation	Mean	SD	Mean	SD	Mean	SD	Mean	SD	Mean	SD	Mean	SD
Aircraft:	DC-8, GV		DC-8, GV		DC-8		DC-8		DC-8, GV		GV	
Obs.	118.7	7.26	0.863	0.272	0.168	0.033	0.174	0.037	0.045	0.037	0.006	0.005
WRF-Chem no scav.	117.9	7.83	1.323	0.414	0.508	0.167	1.480	0.432	0.364	0.088	0.126	0.051
scav. Rvar	117.5	7.88	0.030	0.032	0.360	0.115	0.002	0.009	0.039	0.043	0.074	0.032
scav. R0	117.6	7.90	0.569	0.216	0.359	0.121	0.303	0.162	0.048	0.049	0.078	0.034
scav. R0.25	117.3	8.16	0.036	0.036	0.301	0.099	0.007	0.019	0.042	0.044	0.036	0.014
scav. R0.5	117.9	8.02	0.031	0.033	0.259	0.080	0.003	0.018	0.037	0.043	0.018	0.006
scav. R1	118.1	8.09	0.021	0.025	0.182	0.053	0.001	0.007	0.037	0.043	0.007	0.004

Comparing mean vertical outflow profiles (Figure 4) and mean inflow and outflow values (Table 6) of carbon monoxide (CO) and soluble species from aircraft observations and the different WRF-Chem simulations indicates how well the model is representing entrainment and scavenging. In order to illustrate the vertical variability within the anvil, the model profiles are constructed from all grid points within the latitude-longitude regions of outflow sampling by the two aircraft and the entire vertical extent of the simulated anvil clouds (approximately 7–13 km asl). On the other hand, the model points used to calculate the mean values are restricted to the altitude extents of each aircraft in order to quantitatively compare model and observations. The uncertainties in the mean values are estimated as the standard deviations of the observations and model points, from different spatial locations and times, used to calculate those values. In the future, an ensemble of WRF-Chem simulations, with varying physics and chemistry parameterizations and grid spacings, could be conducted in order to bound the uncertainty in the simulated wet removal.

Carbon monoxide (CO) is used as a passive tracer to examine entrainment, since CO is insoluble and has a long chemical lifetime relative to the timescale of the storm. All six WRF-Chem simulations indicate that mean CO values are within 3% of observed in inflow and within the error bars of the observations in outflow. Since the background CO profile is reinitialized at 21 UTC from observations, the correct WRF-Chem mean inflow and outflow values indicate that the model is representing the transport adequately. However, *Lebo and Morrison* [2015] determined that a horizontal grid spacing of 250 m was necessary for convergence of statistical convective properties and mixing in WRF simulations of idealized squall lines. *Bryan et al.* [2003] and *Bryan and Morrison* [2012] found that entrainment in a numerical model similar to WRF was underestimated at a horizontal grid spacing of 1 km, due to the inability to properly resolve turbulent eddies. Nevertheless, for the WRF-Chem simulations of the present study, the mean free tropospheric entrainment rate of $7.3 \pm 3.3\%$ km^{-1}, determined from simulations of separate passive tracers for each 1 km vertical layer, was consistent with the value of $7.6 \pm 1.6\%$ km^{-1} calculated from hydrocarbon observations [*Barth et al.*, 2016].

Table 7. Scavenging Efficiencies (SE, %) and Uncertainties (δSE, %) for the Oklahoma 29–30 May Storm From Observations and WRF-Chem Simulations

	CH_2O		CH_3OOH		H_2O_2		HNO_3		SO_2	
Species	SE (%)	δSE (%)	SE (%)	δSE (%)	SE (%)	δSE (%)	SE (%)	δSE (%)	SE (%)	δSE (%)
Outflow Aircraft	DC-8, GV		DC-8		DC-8		DC-8, GV		GV	
Obs.	56	11	78	6	86	4	87	17	67	91
WRF-Chem										
scav. Rvar	98	3	29	33	100	1	89	12	41	35
scav. R0	57	21	29	33	80	12	87	14	38	36
scav. R0.25	97	3	41	28	100	1	89	12	71	16
scav. R0.5	98	3	49	23	100	1	90	12	86	8
scav. R1	98	2	64	16	100	0	90	12	95	4

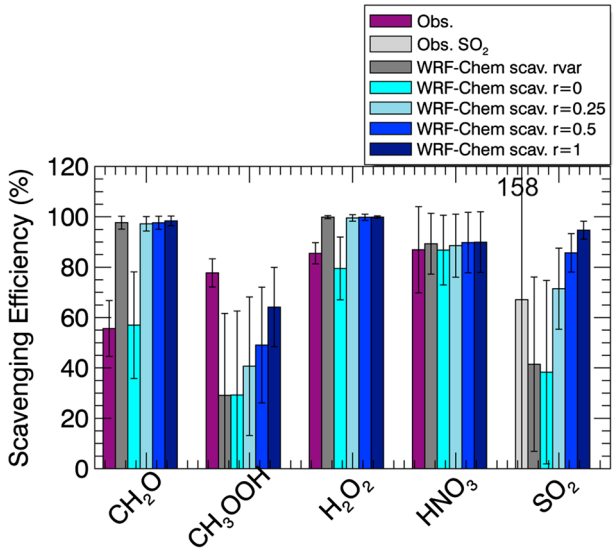

Figure 5. Scavenging efficiencies of soluble species for the Oklahoma 29–30 May storm as observed and from the five WRF-Chem simulations with scavenging. The error bars indicate the error calculated from the standard deviations of the mean values (Tables 6 and 8). Observed SO_2 is in light gray because inflow observations were obtained from DC-8 flights in nearby regions on 19 and 25 May.

For the soluble species, the mean outflow profiles (Figure 4) and values (Table 6) illustrate how much of a gas is removed by scavenging (the difference between the simulation without scavenging and a given simulation with scavenging), as well as the model sensitivity to the ice retention fraction (r_f). The observed and simulated mean inflow values are provided in the supporting information. As a second approach that does not rely on the model having the correct amount of entrainment, we also compare the observed and simulated scavenging efficiencies for the Oklahoma 29–30 May storm (Table 7 and Figure 5). The observed mean *n*-butane mixing ratios and ratios of soluble species to *n*-butane used to calculate the SEs from observations are listed in Table 8. The error propagation analysis used to determine the uncertainties in the scavenging efficiencies, which characterize the range of possible values, is described in the supporting information.

Table 8. Observed Mean *n*-Butane Mixing Ratios (ppb) and Ratios of Selected Soluble Species to *n*-Butane (ppb/ppb) for Storm Case Inflow and Outflow Segments

		n-Butane (ppb)		CH_2O/*n*-Butane (ppb/ppb)		CH_3OOH/*n*-Butane (ppb/ppb)		H_2O_2/*n*-Butane (ppb/ppb)		HNO_3/*n*-Butane (ppb/ppb)		SO_2/*n*-Butane (ppb/ppb)	
Storm/Type	Aircraft	Mean	SD	Mean	SD	Mean	SD	Mean	SD	Mean	SD	Mean	SD
OK 29–30 May													
Inflow S	DC-8	1.548	0.000	2.877	0.217	1.020	0.164	1.627	0.094	0.412	0.036	0.210	0.116
	Aircraft	DC-8, GV		DC-8, GV		DC-8		DC-8		DC-8, GV		GV	
Outflow		0.691	0.182	1.276	0.304	0.227	0.044	0.236	0.067	0.054	0.070	0.069	0.187
AL 21 May													
Inflow	DC-8	0.215	0.038	13.397	2.310	—	—	4.603	1.066	5.797	1.107	1.701	0.286
Outflow	GV	0.127	0.008	2.744	0.499	2.778	0.402	1.552	0.144	1.448	0.327	0.138	0.051
CO 6–7 June													
Inflow	DC-8, GV	0.308	0.025	5.149	0.594	3.578	0.545	13.241	1.389	2.677	0.384	0.199	0.085
	Aircraft	DC-8, GV		DC-8, GV		DC-8		DC-8		DC-8, GV		DC-8, GV	
Outflow		0.299	0.161	1.641	0.698	0.570	0.449	0.412	0.443	0.232	0.568	0.063	0.232
CO 22–23 June S													
Inflow	DC-8	0.194	0.025	8.883	1.123	3.339	0.517	7.793	0.735	1.703	0.299	0.690	0.058
Outflow	DC8	0.154	0.006	4.206	2.644	1.878	0.436	1.457	0.442	0.087	0.199	0.054	0.029

For all soluble species except HNO_3, the outflow profiles are highly sensitive to the r_f values, resulting in near-complete removal for some r_f values and partial removal consistent with observations for other values of r_f. For CH_2O and H_2O_2, only the simulation with scavenging and zero ice retention ($r_f = 0$) produces mean outflow values and SEs (CH_2O: 57% ± 21%, H_2O_2: 80% ± 12%) consistent with observations (CH_2O: 56% ± 11%, H_2O_2: 86% ± 4%). Using any r_f value greater than zero results in near-complete removal (SEs for CH_2O: 97–98%, H_2O_2: 100%). Therefore, including aqueous phase sinks of CH_2O would likely result in too much CH_2O removal, even with zero ice retention. On the other hand, for CH_3OOH, only the scavenging simulation with $r_f = 1$ provides a mean outflow value and scavenging efficiency (64% ± 16%) consistent with the SE from observations (78% ± 6%). The simulated CH_3OOH SEs increase monotonically with the r_f value, ranging from 29 to 49% for r_f of 0–0.5. The WRF-Chem simulations do not include aqueous phase chemistry, except for HSO_3- oxidation by H_2O_2, and we expect both H_2O_2 and CH_3OOH to be depleted in the aqueous phase. Therefore, assuming complete ice retention for CH_3OOH could be compensating for the missing aqueous sink in the model. However, there may be factors other than aqueous chemistry affecting H_2O_2 removal, since we must completely degas H_2O_2 from freezing hydrometeors in order to reproduce the observations.

We have low confidence in the scavenging efficiency for SO_2 since there were no SO_2 inflow measurements on 29–30 May and we used boundary layer observations from flights in Oklahoma on 19 and 25 May to calculate the mean inflow value. Additionally, the GV outflow measurements are highly variable, resulting in a large uncertainty in the SO_2 SE from observations (67% ± 91%). Nevertheless, the mean outflow value for the simulation with complete ice retention ($r_f = 1$, 0.007 ± 0.004 ppb) is within the error bars of the mean outflow value from observations (0.006 ± 0.005 ppb). All other simulations show substantially (200–2000%) higher mean outflow values. However, it is possible that we must assume the maximum value of ice retention for SO_2 to compensate for an insufficient aqueous phase chemical sink in the model. We note that the lower bounds (mean minus uncertainty) of the mean outflow values of HNO_3 are below the detection limits of the instruments. Therefore, if some of the observed outflow values that are below the detection limit have actual values closer to zero, the mean outflow value would be lower and the scavenging efficiency calculated from observations would be closer to one.

For HNO_3, the WRF-Chem scavenging scheme represents dissolution in cloud water, retention in freezing hydrometeors, and direct deposition from the gas phase to ice. The choice of ice retention fraction has little impact on the HNO_3 mean outflow profiles and values or scavenging efficiencies (r_f = 0, 0.25, 0.5, 1; SE = 87% ± 14%, 89% ± 12%, 90% ± 12%, 90% ± 12%), and the SEs from all simulations with scavenging are within the error bars of the SE from observations (SE = 87% ± 17%). Since the lower bounds (mean minus uncertainty) of the mean outflow values of HNO_3 are below the detection limits of the instrument, the true scavenging efficiency may be closer to one. The insensitivity to the r_f value of the simulations with scavenging suggests that mixed-phase scavenging, which includes the ice retention process, plays little role in HNO_3 removal in this storm.

In summary, we are able to simulate the scavenging efficiencies of each soluble species within the uncertainties of the observations by choosing certain values for the ice retention fractions. Notably, we must assume zero retention for CH_2O and H_2O_2, and complete retention for CH_3OOH and SO_2, which may be compensating for the limited (only HSO_3- oxidation by H_2O_2) aqueous chemistry in the model. The ice retention values for H_2O_2 and SO_2 that provide the best agreement with observations in the present study are different from the values of $r_f = 0.64$ for H_2O_2 and $r_f = 0.02$ for SO_2 determined from theory and laboratory observations [*Voisin et al.*, 2000; *von Blohn et al.*, 2011]. However, we have low confidence in the result for SO_2 due to the lack of inflow measurements and the high variability in outflow observations on 29–30 May. Finally, the ice retention fraction has little impact on the simulated scavenging efficiency of HNO_3, indicating that mixed-phase scavenging is not the primary removal process for HNO_3.

3.2.3. Comparison With Previous Studies of Ice Retention

Other modeling studies have found different sensitivities of soluble species SEs to r_f than the present study. For WRF-Chem simulations with r_f values varying from zero to one, we find SEs ranging from 57% to 98% for CH_2O, 29% to 64% for CH_3OOH, and 80% to 100% for H_2O_2. In WRF-AqChem simulations of a Colorado supercell, *Barth et al.* [2007a] calculated much lower SEs for these species, with SEs of 11% and 46% for CH_2O, 1% and 7% for CH_3OOH, and 15% and 58% for H_2O_2 in simulations with zero and complete ice retention, respectively. However, *Barth et al.* [2007a] determined SEs as the ratio of the moles of soluble species deposited at the surface in precipitation to that ingested into the storm. A possible explanation for the lower SEs calculated by *Barth et al.* [2007a] is that their wet deposition SE does not include the fraction of species redistributed

to the midtroposphere, while the SE in the present study would count this fraction as removed since it does not emerge in outflow. Future studies adding the capability to track dissolved species in hydrometeors and thus calculate wet deposition, as well as simulations of Colorado storms, will enable us to directly compare with *Barth et al.* [2007b]. We do see a similar effect of ice retention on CH_2O mixing ratios as in 2-D Meso-NH (a mesoscale nonhydrostatic model) simulations of a tropical squall line by *Leriche et al.* [2013]. In the 2-D squall line case, *Leriche et al.* [2013] found that CH_2O mixing ratios in the stratiform anvil decreased from 150 pptv to 50–100 pptv in simulations with aqueous chemistry when ice retention was included. In our study, CH_2O anvil mixing ratios are 75% lower in the storm simulation with complete ice retention than in the simulation with zero ice retention, while *Leriche et al.* [2013] find 33–67% lower CH_2O anvil mixing ratios in their storm simulation with complete zero ice retention relative to the simulation with zero ice retention.

Both *Barth et al.* [2007a] and the present study found a large increase in H_2O_2 scavenging when ice retention was included. However, *Leriche et al.* [2013] found near-complete removal of H_2O_2 in Meso-NH simulations with and without ice retention of the Colorado supercell also simulated by *Barth et al.* [2007a]. On the other hand, in the Meso-NH Colorado supercell simulations, gas phase mixing ratios of CH_2O in the anvil cloud were lower, and total (gas, liquid, and ice) phase CH_2O mixing ratios were higher, in the simulation with complete ice retention versus the simulation with no ice retention. *Leriche et al.* [2013] attributed the lower sensitivity to ice retention of scavenging of H_2O_2 than CH_2O to the higher-solubility and aqueous phase reactivity of H_2O_2 relative to CH_2O. In the present study, we find that inclusion of ice retention ($r_f \geq 0.25$) increases SEs of both CH_2O and H_2O_2 to near one. Nevertheless, without ice retention ($r_f = 0$), more H_2O_2 is removed (SE = 80% ± 12%) than CH_2O (SE = 57% ± 21%). If we were to include more complete aqueous chemistry in our simulations, other than the simple representation of HSO_3- oxidation by H_2O_2, we would likely see more removal of H_2O_2 and less contrast between the simulations with and without ice retention than in the present study, as in *Leriche et al.* [2013].

3.2.4. Effects of Microphysics and Chemistry on Ice Retention

We now discuss some processes that could affect how SEs respond to different ice retention fractions. The Oklahoma 29–30 May storm had a vertically extensive supercooled region ($\Delta z = 5.78$ km, calculated from the 22:55:59 UTC sounding as the vertical depth from the freezing level to $T = 233.15$ K). Therefore, much of the gas released from freezing hydrometeors could be lofted in updrafts and dissolved in supercooled liquid according to Henry's law and still be removed by the storm. This mechanism may be the reason that all simulations with $r_f > 0$ have CH_2O and H_2O_2 SEs near one. Also, the different gas mixing ratios exiting the storm core could lead to compensating changes in anvil chemistry.

Furthermore, the amount of soluble species in convective outflow can be altered by aqueous chemistry in cloud droplets, which is not represented in these WRF-Chem simulations, other than HSO_3- oxidation by H_2O_2. CH_2O becomes aqueous $CH_2(OH)_2$ and then can react with HO to produce formic acid (HCOOH) or with S(IV) [*Pandis and Seinfeld*, 1989; *Barth et al.*, 2003, 2007a]. Modeling studies [*Jacob*, 1986; *Lelieveld and Crutzen*, 1990; *Barth et al.*, 2003, 2007a] show decreases in total CH_2O due to aqueous chemistry. However, field observations of CH_2O in the U.S. [*Facchini et al.*, 1992; *Munger et al.*, 1995; *Keene et al.*, 1995; *Fried et al.*, 2008, under review, 2016] have not found this depletion in the presence of clouds. Gas phase production of CH_2O from alkane oxidation was found to offset aqueous phase depletion of CH_2O when nonmethane hydrocarbon (NMHC) chemistry was added to box model simulations of stratus clouds in midlatitude summer conditions [*Barth et al.*, 2003]. The MOZART gas phase mechanism used in the current study includes NMHC production of CH_2O, and near-complete removal of CH_2O is seen for $r_f > 0$. Therefore, if we were to include the aqueous phase reactions of CH_2O with HO and S(IV), simulated CH_2O SEs would likely be too high even using an r_f value of 0. In the aqueous phase, H_2O_2 is consumed by reactions with the bisulfite ion (HSO_3^-), the only aqueous phase reaction represented in the MOZCART chemical mechanism and aerosol scheme, and with HO and produced by the reaction of HO_2^- with the superoxide anion (O_2^-). CH_3OOH can be destroyed in the aqueous phase by reaction with HSO_3^-, and with HO to form either the methyl peroxy radical (CH_3OO) or a diol ($CH_2(OH)_2$), and is produced in the aqueous phase from CH_3OO. If SO_2 mixing ratios are low, there may be some compensation due to production from HO_2^- of the depletion of H_2O_2 by reaction with HSO_3^-. Nevertheless, we still expect H_2O_2, and possibly CH_3OOH, to decrease due to aqueous chemistry. Therefore, the r_f value of 1 found for CH_3OOH may be compensating for the lack of aqueous phase sink in the model. On the other hand, as for CH_2O, including the aqueous phase reaction of H_2O_2 with HO would likely result in too much removal even using an r_f value of 0. For SO_2, including additional aqueous phase oxidation of HSO_3^- or SO_4^{2-} by O_3 or O_2 in

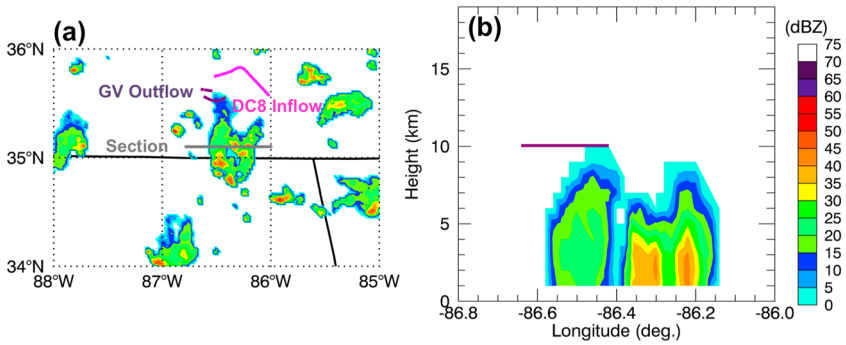

Figure 6. (a) NEXRAD column-maximum radar reflectivity contours (dB*Z*) and (b) east-west vertical reflectivity cross section at the location shown by the gray line in Figure 6a, over Alabama at 2115 UTC on 21 May 2012. Flight segments for DC-8 inflow (magenta) and GV outflow (purple) sampling are indicated by lines. In Figure 6b, the longitudinal and altitude extent of the GV (purple) outflow sampling flight segments is designated by a rectangle.

the WRF-Chem simulations would likely increase the scavenging efficiency values of SO_2, so that ice retention coefficients of less than one could produce the observed amount of wet removal. Finally, aqueous NMHC chemistry provides additional sources of HO_x precursors and can also affect droplet pH [*Carlton et al.*, 2007], but its net impact on abundances of these soluble species is not clear.

The effects of aqueous phase and anvil chemistry on the vertical distribution of soluble species will be investigated in a future study. Simulations with WRF-Chem MOSAIC incorporating aqueous chemistry, as well as simulations of other storm cases with both inflow and outflow observations of SO_2, will enable more precise and confident estimates of ice retention coefficients and wet removal.

4. Comparison of Observed Scavenging in Oklahoma, Alabama, and Colorado Storms

The final objective of this study is to examine storms in Alabama and Colorado to see whether similar amounts of scavenging occur as in the Oklahoma storm. We provide an overview of the Alabama and Colorado storms, followed by the scavenging efficiencies calculated for these storms in relation to the Oklahoma 29–30 May storm, and a comparison with other studies.

4.1. Observations of Alabama and Colorado Storms

On 21 May 2012, convective updrafts triggered by a prefrontal trough initiated at around 1945 UTC in northern Alabama. These updrafts later developed into the discrete ordinary (air mass) convective storm observed by aircraft. A University of Alabama, Huntsville (UAH), mobile RAwinsonde OBservation (RAOB) at 2037 UTC near Capshaw, Alabama, showed a low CAPE value of approximately 785 J kg^{-1} and weak 0–6 km shear of 1.54 m s^{-1}. The storm was observed by the UAH/WHNT-TV-ARMOR dual-pol C-Band Doppler radar from 1950 to 2130 UTC and Alabama LMA and traveled to the E/SE until it dissipated around 21 UTC, with peak updrafts of approximately 10 m s^{-1} [*Mecikalski et al.*, 2015]. The storm formed in a region with a relatively low ratio of anthropogenic to biogenic emissions (20 pptv toluene/360 pptv isoprene observed in the PBL) [*Barth et al.*, 2015]. Figure 6 depicts NEXRAD maximum reflectivities at the end of the inflow and outflow sampling periods, the inflow and outflow flight tracks, and a vertical reflectivity cross section through the storm core at the outflow sampling time. The storm was relatively weak and shallow, with a vertical extent of around 10 km and reflectivities of approximately 50 dB*Z* in the core extending up to only around 5 km asl.

On 6–7 June 2012, the DC-8 and GV sampled inflow and outflow from two cells in NE Colorado that triggered due to the combination of southeasterly moisture flow and northwesterly low level convergence. The prestorm sounding at 21 UTC showed relatively high CAPE of 2981 J kg^{-1} and 0–6 km shear of 34 m s^{-1}. Toluene mixing ratios of approximately 30 pptv and isoprene of 40 pptv were observed in the PBL, suggesting moderate anthropogenic and low biogenic emissions [*Barth et al.*, 2015]. Maximum updraft speeds of 15–40 m s^{-1} for the northern cell and 5–40 m s^{-1} for the southern cell were observed by the CSU-CHILL (S-band and X-band) and CSU-PAWNEE (S-band) dual-pol system [*Basarab et al.*, 2015]. In Figure 7, NEXRAD column-maximum radar reflectivity and a vertical reflectivity cross section at the end of the outflow sampling period show a convective core extending to 15 km asl, with reflectivity in the core attaining 70 dB*Z*.

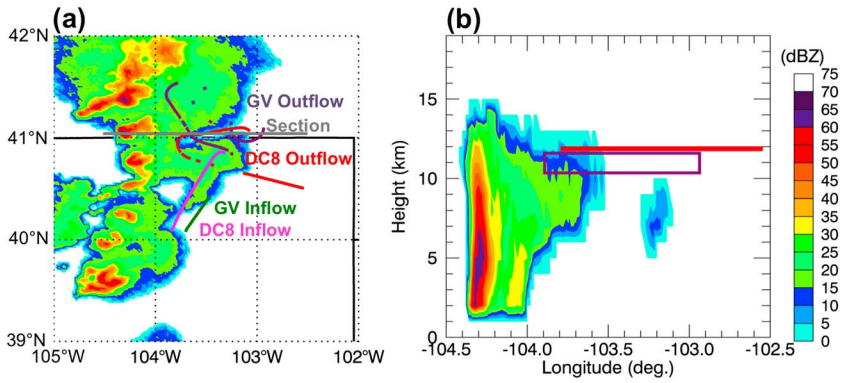

Figure 7. (a) NEXRAD column-maximum radar reflectivity contours (dB*Z*) and (b) east-west vertical reflectivity cross section at the location shown by the gray line in Figure 7a, over Colorado at 0010 UTC on 7 June 2012. Flight segments for DC-8 inflow (magenta) and outflow (red) sampling are indicated by lines. In Figure 7b, the longitudinal and altitude extents of the GV (purple) and DC-8 (red) outflow sampling flight segments are designated by rectangles.

On 22 June 2012, three supercell storms were triggered in NE Colorado by a leeside trough in an environment of S/SE flow. A prestorm sounding at 22 UTC showed a relatively high CAPE of 2563 J kg^{-1} and elevated 0–6 km shear of 24 m s^{-1}. Toluene mixing ratios of approximately 15 pptv and isoprene of 20 pptv were observed in the PBL [*Barth et al.*, 2015], indicating both low anthropogenic and biogenic emissions. In this study, we considered the southern of the two largest storms, which formed near Fort Morgan, CO, around 2330 UTC. The northern cell began to ingest smoke from the High Park Fire at a height of about 7 km at around 0000 UTC. The outflow period for the southern storm was selected to minimize fire influence in scavenging results (A. Fried et al., under review, 2016). The storms tracked into SW Nebraska and were in CHILL and LMA range until approximately 2345 and 0050 UTC for the N and S storms, respectively [*Basarab et al.*, 2015]. Figure 8 shows NEXRAD column-maximum radar reflectivity and vertical reflectivity cross sections of the southern storm at the end of its outflow sampling period. The storm had a high vertical extent (maximum height of approximately 18 km asl) with moderate reflectivity (up to 60 dB*Z*) in its core.

4.2. Comparison of SEs in Oklahoma, Alabama, and Colorado Storms

We now compare SEs calculated from observations of the four DC3 case study storms (Table 9 and Figure 9) to determine the degree to which the amount of scavenging varies among storms that formed in different regions. The observed mean *n*-butane mixing ratios and ratios of other species to *n*-butane for inflow and outflow sampling used to calculate the SEs for the Alabama and Colorado case study storms are listed in Table 8. Differences in SEs among different storm cases are deemed significant if the error bars, defined as the mean values plus and minus the uncertainties, do not overlap. If a difference is significant, the percent difference is listed in Table 9. The mean mixing ratios of the soluble species in inflow and outflow for the Alabama and Colorado cases are given in the supporting information.

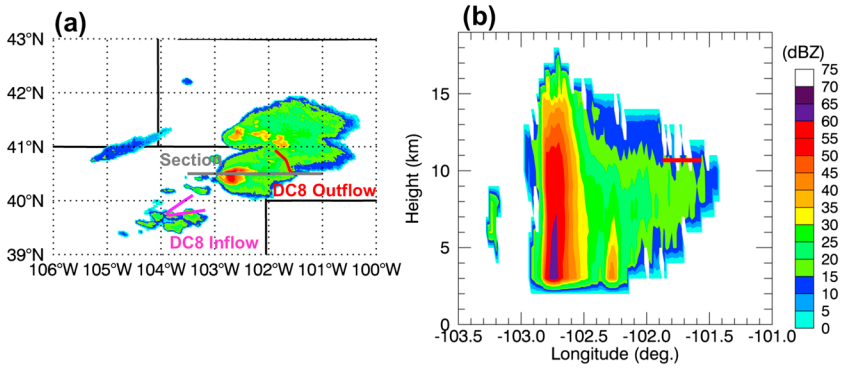

Figure 8. (a) NEXRAD column-maximum radar reflectivity contours (dB*Z*) and (b) east-west vertical reflectivity cross sections at the locations shown by the gray line in Figure 8a, over NE Colorado/SW Nebraska at 0120 UTC on 23 June 2012. Flight segments for DC-8 inflow (magenta) and outflow (red) sampling are shown by lines. In Figure 8b, the longitudinal and altitude extent of the DC-8 (red) outflow sampling flight segments is designated by a rectangle.

Table 9. Observed Scavenging Efficiencies (SE, %) and Uncertainties (δSE, %) for Alabama and Colorado Storm Cases[a]

Species	*n*-Butane		CH_2O		CH_3OOH		H_2O_2		HNO_3		SO_2	
Storm	SE (%)	δSE (%)	SE (%)	δSE (%)	SE (%)	δSE (%)	SE (%)	δSE (%)	SE (%)	δSE (%)	SE (%)	δSE (%)
OK 29–30 May	55	12	56	11	78	6	86	4	87	17	67	91
AL 21 May	41	11	80	5	—	—	66	8	75	7	92	3
% diff OK 29 May	—		43		—		-22		—		—	
CO 6–7 June	3	53	68	14	84	13	97	3	91	21	68	117
% diff OK 29 May	—		—		—		13		—		—	
% diff AL 21 May	—		—		—		13		—		—	
CO 22–23 June S	21	11	53	30	44	16	81	6	95	12	92	4
% diff OK 29 May	−63		—		−44		—		—		—	
% diff AL 21 May	—		—		—		23		27		—	
% diff CO 6 June	—		—		−48		−16		—		—	

[a]Percent differences between storms are listed if significant.

The Oklahoma 29 May and Alabama 21 May storms have higher SEs for *n*-butane (55% ± 12% and 41% ± 11%, respectively) than the Colorado 6 June and 22–23 June S storms (SE = 3% ± 53% and 21% ± 10%, respectively). As previously mentioned in section 2.4, higher *n*-butane "scavenging efficiencies" indicate more entrainment.

We find significant differences in scavenging efficiencies between some storms for all soluble species except SO_2. The observed SEs range from 53 to 80% for CH_2O, 44 to 84% for CH_3OOH, 66 to 97% for H_2O_2, 75 to 95% for HNO_3, and 67 to 92% for SO_2. For CH_2O, the Alabama 21 May storm removes 43% more CH_2O (SE = 80% ± 5%) than the Oklahoma 29–30 May storm (SE = 56% ± 11%). For H_2O_2, Oklahoma 29–30 May (SE = 86% ± 4%) and Colorado 6 June (97% ± 3%) remove more than the Colorado 22–23 June S (81% ± 6%) and Alabama 21 May (SE = 66% ± 8%) storms. Similarly, there is higher removal of CH_3OOH by the Oklahoma 29–30 May (78% ± 6%) and Colorado 6 June (84% ± 13%) storms than in the Colorado 22–23 June S (44% ± 16%) storm. However, there were no CH_3OOH measurements during the Alabama 21 May inflow sampling period. For HNO_3 a larger SE is calculated for the Colorado 22–23 June S (95% ± 12%) storm than in the Alabama 21 May (75% ± 7%) storm, while Oklahoma (87% ± 17%) and Colorado 6 June (91% ± 21%) each overlap all the other cases.

For SO_2, the differences between the SEs (67% to 92%) are not significant because the error bars are large for the two storms with the lowest SEs, Oklahoma (67% ± 91%) and Colorado 6 June (68% ± 117%). The large error bars are due to the high variability in both inflow and outflow. In addition, inflow data were obtained

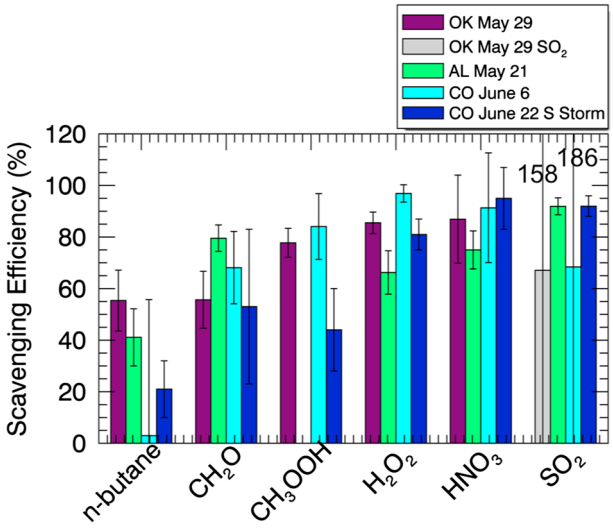

Figure 9. Scavenging efficiencies of *n*-butane and soluble species for the four DC3 case study storms. The error bars indicate the error calculated from the standard deviation of the mean values (Table 8). Observed SO_2 for the 29–30 May case is in light gray because inflow observations were obtained from DC-8 flights in nearby regions on 19 and 25 May.

from DC-8 measurements on 19 and 25 May in nearby, but different, locations. Thus, we have low confidence in the SE for SO_2 for the Oklahoma and Colorado 6 June storms.

We note that the lower bounds (mean minus uncertainty) of some of the mean outflow values of HNO_3 and SO_2 are below the detection limits of the instruments. These include the 29–30 May, 6 June, and 22–23 June S storms for HNO_3 and the 29–30 May, 21 May, and 6 June storms for SO_2. Therefore, if some of the observational values below the detection limit are actually closer to zero, the true SEs would be closer to one.

4.3. Comparison of Scavenging Efficiencies With Other Studies

Two other studies have examined scavenging efficiencies of soluble gases in DC3 storms. A. Fried et al. (under review, 2016) calculated CH_2O SEs with the *n*-butane ratio method and also an altitude-dependent entrainment model, using outflow observations extrapolated to the top of the storm core. *Barth et al.* [2016] determined CH_3OOH and H_2O_2 scavenging efficiencies using an altitude-dependent entrainment model, utilizing outflow measurements directly as in the present study. A. Fried et al. (under review, 2016) and *Barth et al.* [2016] include SEs calculated from the same WRF-Chem simulations of the present study but calculated from the difference of values at the top of the storm core (40 dB*Z* contour) in simulations with and without scavenging.

For CH_2O, extrapolating outflow observations to the storm core will result in lower SEs as CH_2O has gas phase chemical sources and sinks that can cause their mixing ratios in outflow to change downwind of the core. For example, the mean CH_2O/*n*-butane ratio in outflow is 1.276 in the present study, compared with the value of 1.42 extrapolated to the top of the storm core by A. Fried et al. (under review, 2016). The resulting CH_2O SEs are 56% from observations and 57% from the WRF-Chem simulation without ice retention in the present study and 51% from observations extrapolated to the top of the storm core and 53% from the WRF-Chem simulation without ice retention using outflow values from the 40 dB*Z* contour in A. Fried et al. (under review, 2016). The CH_2O scavenging efficiencies from the present study and A. Fried et al. (under review, 2016) calculated from observations and the WRF-Chem simulation without ice retention all agree within the uncertainties.

The present study and A. Fried et al. (under review, 2016) both found a higher CH_2O SE for the Alabama 21 May storm (80% ± 5% and 81% ± 5%, respectively) than the Oklahoma 29–30 May storm (56% ± 11% and 51% ± 5–6%, respectively). However, we point out that A. Fried et al. (under review, 2016) had less confidence in the Alabama 21 May result because they determined using hydrocarbon observations that the inflow and outflow air were not of the same origin.

While the present study finds more peroxide removal in the Oklahoma 29–30 May than Colorado 22–23 June S storms, *Barth et al.* [2016] do not find significantly different SEs among the Oklahoma 29 May, Colorado 6 June, and Colorado 22 June S storms (CH_3OOH: 44–85%, H_2O_2: 79–97%). However, the error bars are larger for *Barth et al.* [2016] because they calculate the uncertainty in SEs from the average measurement uncertainty, while the present study uses the standard deviation of the measurements (variability). The WRF-Chem simulations with the same r_f values as in the present study provide SEs (calculated from outflow values at the 40 dB*Z* contour) that agree with the SEs calculated from observations for CH_3OOH ($r_f = 0$) and H_2O_2 ($r_f = 1$).

Several studies have estimated scavenging efficiencies for soluble gases from aircraft observations in other regions of the world. All DC3 CH_2O SEs are higher than the values of 4–39% calculated from observations of deep convection in West Africa by *Borbon et al.* [2012] using a three-component (PBL/FT/UT) mixture model. The DC3 peroxide SEs are higher than those found for marine deep convection over the South Pacific by *Cohan et al.* [1999], who determined SEs of 55–70% for H_2O_2 and negligible removal of CH_3OOH using a two-component mixture model (PBL/UT). The differences in SEs calculated from these three field campaigns suggest that differences among storms may exist among regions of the globe as well as within the Central U.S. and should be investigated in a future study.

Since *n*-butane is not expected to be removed in the cloud, its SE corresponds to an entrainment rate. Therefore, the storms with the highest SEs for *n*-butane in the present study also have the highest entrainment rates calculated from hydrocarbon measurements in A. Fried et al. (under review, 2016), indicating that the ratio of *n*-butane in outflow and inflow is a good proxy for the amount of dilution with free tropospheric air. The Oklahoma 29 May and Alabama 21 May storms have the highest SEs (55% ± 12% and 41% ± 11%, respectively) and also the highest entrainment rates integrated from 1 to 10 km (inflow and outflow altitudes), (68 ± 10% and 80 ± 24%, respectively). On the other hand, the Colorado 6 June and 22–23 June S storms

have both the lowest SEs (3% ± 53% and 21% ± 10%, respectively) and 1–10 km entrainment rates (37 ± 6% and 32 ± 11% km^{-1}, respectively). A. Fried et al. (under review, 2016) used *i*-butane, *n*-pentane, and *i*-pentane, as well as *n*-butane, to calculate the entrainment rates, which may explain the discrepancies between the present study and A. Fried et al. (under review, 2016) in the entrainment rates for the Alabama storm.

4.4. Microphysical Factors Contributing to Observed Differences in Scavenging Among Storms

We now discuss whether differences in dynamical and microphysical properties among storms could explain some of the observed differences in removal of soluble gases. *Barth et al.* [2016] found a negative correlation of CH_3OOH scavenging with entrainment rate for six DC3 storms, including the Oklahoma and Colorado storms in the present study. However, the Colorado 22–23 June S storm has a similar entrainment rate to the Colorado 6 June storm but much lower SEs for CH_3OOH (44% ± 16% versus 84% ± 13%). Therefore, entrainment alone does not explain the difference between the Colorado 6–7 and 22–23 June S storms in CH_3OOH scavenging.

Barth et al. [2016] also explored whether lightning NO_x production could increase CH_3OOH scavenging by decreasing gas phase production of CH_3OOH from $CH_3OO + HO_2$. Using reaction rates and aircraft HO_2 and NO_x observations, they found higher CH_3OOH removal with a lower fraction of CH_3OO producing CH_3OOH. However, the cloud parcel model employed by *Barth et al.* [2016] did not show an effect of lightning NO_x emissions on CH_3OOH scavenging. Lightning flashes are associated with graupel mass and thus may indicate the amount of mixed-phase scavenging. More mixed-phase scavenging in the Oklahoma storm, with a maximum flash rate of 312 flashes min^{-1} (K. Cummings et al., in preparation, 2016b), than in the Colorado 22–23 June S storm, with a maximum flash rate of 140.4 flashes min^{-1} [*Basarab et al.*, 2015], may explain the higher CH_3OOH SE for the Oklahoma storm than the Colorado 22–23 June S storm. However, the Colorado 6 June storm has a substantially lower maximum flash rate of 87.5 flashes min^{-1} [*Basarab et al.*, 2015] yet an equivalent CH_3OOH SE to the Oklahoma storm. The lack of a clear dependence of CH_3OOH SE on flash rate indicates that other factors, such as the amount of liquid versus mixed-phase removal, may contribute to the amount of CH_3OOH scavenging in the Oklahoma and Colorado 6–7 June cases. The greater removal in the Colorado 22 June S storm compared to the Alabama storm may be due to higher graupel content in the Colorado 22 June S storm, which had a much higher maximum flash rate of 140.4 min^{-1} for the Colorado 22 June S storm [*Basarab et al.*, 2015] versus 5 min^{-1} for the Alabama storm [*Mecikalski et al.*, 2015].

In future studies, graupel amount could be estimated using polarimetric radar hydrometeor retrievals. The observed hydrometeor distributions could be analyzed together with WRF-Chem simulations of the Alabama and Colorado cases in order to determine whether the observed variability among storms in the amount of wet scavenging are due to different microphysical characteristics of the storms. WRF-Chem simulations could also be used to study the sensitivity of soluble gas scavenging to chemical sources and sinks such as aqueous chemistry and lightning NO_x production. We note that the physics of freezing of hydrometeors is not well understood. Since the fractions retained of soluble gases when hydrometeors freeze have been found to vary with microphysical factors such as drop size and temperature and the air speed around the drop [*Stuart and Jacobson*, 2004], the simulated amount of trace gas scavenging is dependent upon the representation of ice physics in the models.

5. Conclusions

The DC3 field campaign was the first to observe thunderstorms in the Central U.S. with a full suite of trace gas measurements in conjunction with ground-based soundings, radar, and lightning observations. Thus, DC3 offers an unprecedented opportunity to study the role of wet scavenging in the tropospheric distribution of soluble species.

The first two objectives of this study were to examine how well a simple wet scavenging scheme in a cloud-resolving chemistry-meteorology model represents wet removal in one of the case study DC3 storms and to estimate the fraction of different soluble species retained in ice. High-resolution ($\Delta x = 1$ km) WRF-Chem simulations of the Oklahoma 29 May 2012 storm demonstrate the ability of WRF-Chem to represent thunderstorm dynamics and tracer transport. A new capability was added to WRF-Chem to vary the ice retention fraction (r_f) by species, and sensitivity simulations were conducted to determine the ice retention fraction for each species. The scavenging efficiencies of all species except HNO_3 are highly sensitive to

their ice retention fraction. If we assume zero ice retention for CH_2O and H_2O_2 and complete ice retention for CH_3OOH and SO_2, we simulate the outflow trace gas mixing ratios within the error bars of the observations.

Theory and laboratory observations [e.g., *Voisin et al.*, 2000; *von Blohn et al.*, 2011] indicate that CH_2O, CH_3OOH, H_2O_2, and SO_2 should be partially retained in ice. These four species are known to have aqueous chemistry sources and sinks [*Pandis and Seinfeld*, 1989], which are not included in these simulations. Previous modeling studies of a Colorado supercell [*Barth et al.*, 2007b; *Leriche et al.*, 2013] found a high sensitivity of CH_2O and CH_3OOH scavenging efficiencies to their ice retention fraction but disagree on whether H_2O_2 removal is dominated by aqueous sinks or mixed-phase scavenging. Thus, ongoing work includes exploring whether the simulations are missing net chemical sources or sinks to the gas phase and/or overestimating the amount of ice phase hydrometeors, requiring us to compensate by ejecting all CH_2O and H_2O_2 from ice and completely retaining CH_3OOH and SO_2. We also note that although no conclusions can be drawn about retention of HNO_3 in freezing hydrometeors, mixed-phase scavenging does not appear to be a strong factor in the overall removal rate.

The third objective of this study was to use the aircraft observations to examine how much wet removal varies among storms with distinct dynamical and emissions characteristics. SEs for the Oklahoma 29–30 May storm were compared with DC3 observations of a discrete ordinary convective storm in Alabama on 21 May 2012, severe convection in NE Colorado on 6–7 June 2012, and a supercell in NE Colorado/SW Nebraska on 22–23 June 2012. The SEs calculated in the present study are consistent with those found using different methods for CH_2O by A. Fried et al. (under review, 2016) and for the peroxides by *Barth et al.* [2016]. The SEs from all three studies are higher than those calculated from observations from West Africa and the South Pacific [*Cohan et al.*, 1999; *Borbon et al.*, 2012]. Significant differences in SEs are seen between some storms for all species except SO_2. Less scavenging of CH_3OOH and more removal of HNO_3 are seen in storms with higher maximum flash rates, an indication of more graupel mass. Graupel is associated with mixed-phase scavenging and lightning NO_x production, processes that may explain the observed differences in HNO_3 and CH_3OOH scavenging among the Oklahoma, Alabama, and Colorado 22–23 June S storms.

The advantage of the NP2012 scheme is that wet removal can be parameterized without needing to add additional variables predicting the amount of trace gases in different cloud particles. However, without estimates of dissolved trace gases in the liquid water or ice, multiphase chemistry cannot be well represented. Therefore, next steps include high-resolution simulations with MOSAIC aerosols and aqueous chemistry of the Oklahoma, Alabama, and Colorado cases to determine if the model captures the observed variability in wet removal, as well as whether better estimates of ice retention factors can be made. In addition, tracking dissolved species in different hydrometeor types and comparison of simulated and radar-retrieved hydrometeor distributions will enable us to quantify the relative contribution of aqueous chemistry and microphysical processes on the observed vertical distribution of soluble species. Thus, the unique measurements from DC3 teamed with a detailed representation of wet removal and convective transport will provide methods for improved parameterization of convective transport and scavenging in air quality and climate models.

Acknowledgments

We express our appreciation to the following researchers for the aircraft observations: T. Ryerson and the NOAA NO_yO_3 team; Andrew Weinheimer; Mark Zondlo, Josh DiGangi, and Anthony O'Brien for the VCSEL hygrometer water vapor measurements on the GV; and P. Lawson and S. Woods from SPEC Inc. We also thank A. Weinheimer and M. Zondlo for their helpful feedback on this manuscript. M.M. Bela and O.B. Toon were supported by NASA ACCDAMNNX14AR56G. The National Center for Atmospheric Research is sponsored by the National Science Foundation. A. Fried was supported by NSF and NASA under grants AGS-1261559 and NNX12AMO8G, respectively. C. Homeyer was funded by NSF grant AGS-1522910. The University of Maryland co-authors were supported under NSF grants 1063479 and 1522551. Q. Yang was supported by the Office of Science of the U.S. Department of Energy as part of the Atmospheric System Research Program (ASR). P.O. Wennberg, J.D. Crounse, A.P. Teng, and J.M. St. Clair thank NASA for supporting their contribution to this study (NNX12AC06G and NNX14AP46G-ACCDAM). D. O'Sullivan thanks NSF for support from grant ATM1063467. L.G. Huey, D. Chen, and X. Liu were funded by NASA grant NNX12AB77G. DC3 measurements by N. Blake and D. Blake were supported by NASA award NNX12AB76G. We would like to thank Earth Networks for providing the ENTLN lightning data for research purposes. The data used in this study can be downloaded from the following websites: 1 s data merges from the NASA Langley DC3 Merged Aircraft Dataset Archive (http://www-air.larc.nasa.gov/cgi-bin/ArcView/dc3); NEXRAD data for individual radars from the National Climatic Data Center (NCDC; http://has.ncdc.noaa.gov/pls/plhas/has.dsselect); NSSL-MGAUS sounding data (http://data.eol.ucar.edu/codiac/dss/id=353.105); NCEP Stage IV precipitation analysis (http://www.emc.ncep.noaa.gov/mmb/ylin/pcpanl/stage4/); and NAM-ANL (http://nomads.ncdc.noaa.gov/data/namanl/). The WRF-Chem code and land surface data are available for download from NCAR/MMM (http://www.mmm.ucar.edu/wrf/users/download/get_sources_wps_geog.html). WRF-Chem model output is available upon request to M.M. Bela (megan.bela@colorado.edu).

References

Abbatt, J. P. D. (1997), Interaction of HNO_3 with water-ice surfaces at temperatures of the free troposphere, *Geophys. Res. Lett.*, *24*(12), 1479–1482, doi:10.1029/97GL01403.

Alexander, B., R. J. Park, D. J. Jacob, Q. B. Li, R. M. Yantosca, J. Savarino, C. C. W. Lee, and M. H. Thiemens (2005), Sulfate formation in sea-salt aerosols: Constraints from oxygen isotopes, *J. Geophys. Res.*, *110*, D10307, doi:10.1029/2004JD005659.

Alexander, B., R. J. Park, D. J. Jacob, and S. Gong (2009), Transition metal-catalyzed oxidation of atmospheric sulfur: Global implications for the sulfur budget, *J. Geophys. Res.*, *114*, D02309, doi:10.1029/2008JD010486.

Alexander, B., D. J. Allman, H. M. Amos, T. D. Fairlie, J. Dachs, D. A. Hegg, and R. S. Sletten (2012), Isotopic constraints on the formation pathways of sulfate aerosol in the marine boundary layer of the subtropical northeast Atlantic Ocean, *J. Geophys. Res.*, *117*, D06304, doi:10.1029/2011JD016773.

Amelynck, C., N. Schoon, and E. Arijs (2000), Gas phase reactions of CF_3O^- and CF_3OH_2O with nitric, formic, and acetic acid, *Int. J. Mass. Spectrom.*, *203*(1–3), 165–175, doi:10.1016/S1387-3806(00)00321-3.

Apel, E. C., et al. (2015), Upper tropospheric ozone production from lightning NO_x-impacted convection: Smoke ingestion case study from the DC3 campaign, *J. Geophys. Res. Atmos.*, *120*, 2505–2523, doi:10.1002/2014JD022121.

Barth, M. C. (2006), The importance of cloud drop representation on cloud photochemistry, *Atmos. Res.*, *82*(1–2), 294–309, doi:10.1016/j.atmosres.2005.10.008.

Barth, M. C., A. L. Stuart, and W. C. Skamarock (2001), Numerical simulations of the July 10, 1996, Stratospheric-Tropospheric Experiment: Radiation, Aerosols, and Ozone (STERAO)-Deep Convection experiment storm: Redistribution of soluble tracers, *J. Geophys. Res.*, *106*(D12), 12,381–12,400, doi:10.1029/2001JD900139.

Barth, M. C., S. Sillman, R. Hudman, M. Z. Jacobson, C.-H. Kim, A. Monod, and J. Liang (2003), Summary of the cloud chemistry modeling intercomparison: Photochemical box model simulation, *J. Geophys. Res.*, *108*(D7), 4214, doi:10.1029/2002JD002673.

Barth, M. C., S.-W. Kim, W. C. Skamarock, A. L. Stuart, K. E. Pickering, and L. E. Ott (2007a), Simulations of the redistribution of formaldehyde, formic acid, and peroxides in the 10 July 1996 Stratospheric-Tropospheric Experiment: Radiation, Aerosols, and Ozone deep convection storm, *J. Geophys. Res.*, *112*, D13310, doi:10.1029/2006JD008046.

Barth, M. C., et al. (2007b), Cloud-scale model intercomparison of chemical constituent transport in deep convection, *Atmos. Chem. Phys.*, *7*(18), 4709–4731, doi:10.5194/acp-7-4709-2007.

Barth, M. C., J. Lee, A. Hodzic, G. Pfister, W. C. Skamarock, J. Worden, J. Wong, and D. Noone (2012), Thunderstorms and upper troposphere chemistry during the early stages of the 2006 North American Monsoon, *Atmos. Chem. Phys.*, *12*(22), 11,003–11,026, doi:10.5194/acp-12-11003-2012.

Barth, M. C., et al. (2015), The Deep Convective Clouds and Chemistry (DC3) field campaign, *Bull. Am. Meteorol. Soc.*, *96*(8), 1281–1309, doi:10.1175/BAMS-D-13-00290.1.

Barth, M. C., et al. (2016), Convective transport of peroxides by thunderstorms observed over the Central U.S. during DC3, *J. Geophys. Res. Atmos.*, doi:10.1002/2015JD024570.

Basarab, B. M., S. A. Rutledge, and B. R. Fuchs (2015), An improved lightning flash rate parameterization developed from Colorado DC3 thunderstorm data for use in cloud-resolving chemical transport models, *J. Geophys. Res. Atmos.*, *120*, 9481–9499, doi:10.1002/2015JD023470.

Bertram, T. H., et al. (2007), Direct measurements of the convective recycling of the upper troposphere, *Science*, *315*(5813), 816–820, doi:10.1126/science.1134548.

Betts, A. K., L. V. Gatti, A. M. Cordova, M. A. F. Silva Dias, and J. D. Fuentes (2002), Transport of ozone to the surface by convective downdrafts at night, *J. Geophys. Res.*, *107*(D20), 8046, doi:10.1029/2000JD000158.

Blake, N. J., et al. (2003), NMHCs and halocarbons in Asian continental outflow during the Transport and Chemical Evolution over the Pacific (TRACE-P) field campaign: Comparison with PEM-West B, *J. Geophys. Res.*, *108*(D20), 8806, doi:10.1029/2002JD003367.

Boccippio, D. J., K. L. Cummins, H. J. Christian, and S. J. Goodman (2001), Combined satellite- and surface-based estimation of the intracloud–cloud-to-ground lightning ratio over the continental United States, *Mon. Weather Rev.*, *129*(1), 108–122, doi:10.1175/1520-0493(2001)129<0108:CSASBE>2.0.CO;2.

Borbon, A., et al. (2012), Transport and chemistry of formaldehyde by mesoscale convective systems in West Africa during AMMA 2006, *J. Geophys. Res.*, *117*, D12301, doi:10.1029/2011JD017121.

Bryan, G. H., and H. Morrison (2012), Sensitivity of a simulated squall line to horizontal resolution and parameterization of microphysics, *Mon. Weather Rev.*, *140*(1), 202–225, doi:10.1175/MWR-D-11-00046.1.

Bryan, G. H., J. C. Wyngaard, and J. M. Fritsch (2003), Resolution requirements for the simulation of deep moist convection, *Mon. Weather Rev.*, *131*(10), 2394–2416, doi:10.1175/1520-0493(2003)131<2394:RRFTSO>2.0.CO;2.

Carlton, A. G., B. J. Turpin, K. E. Altieri, S. Seitzinger, A. Reff, H.-J. Lim, and B. Ervens (2007), Atmospheric oxalic acid and SOA production from glyoxal: Results of aqueous photooxidation experiments, *Atmos. Environ.*, *41*(35), 7588–7602, doi:10.1016/j.atmosenv.2007.05.035.

Chatfield, R. B., and P. J. Crutzen (1984), Sulfur dioxide in remote oceanic air: Cloud transport of reactive precursors, *J. Geophys. Res.*, *89*(D5), 7111–7132, doi:10.1029/JD089iD05p07111.

Chin, M., P. Ginoux, S. Kinne, O. Torres, B. N. Holben, B. N. Duncan, R. V. Martin, J. A. Logan, A. Higurashi, and T. Nakajima (2002), Tropospheric aerosol optical thickness from the GOCART model and comparisons with satellite and Sun photometer measurements, *J. Atmos. Sci.*, *59*(3), 461–483, doi:10.1175/1520-0469(2002)059<0461:TAOTFT>2.0.CO;2.

CISL (2012), *Yellowstone: IBM iDataPlex System (NCAR Community Computing)*, Natl. Cent. Atmos. Res., Boulder, Colo.

Cohan, D. S., M. G. Schultz, D. J. Jacob, B. G. Heikes, and D. R. Blake (1999), Convective injection and photochemical decay of peroxides in the tropical upper troposphere: Methyl iodide as a tracer of marine convection, *J. Geophys. Res.*, *104*(D5), 5717–5724, doi:10.1029/98JD01963.

Cooper, O. R., et al. (2006), Large upper tropospheric ozone enhancements above midlatitude North America during summer: In situ evidence from the IONS and MOZAIC ozone measurement network, *J. Geophys. Res.*, *111*, D24S05, doi:10.1029/2006JD007306.

Crounse, J. D., K. A. McKinney, A. J. Kwan, and P. O. Wennberg (2006), Measurement of gas-phase hydroperoxides by chemical ionization mass spectrometry, *Anal. Chem.*, *78*(19), 6726–6732, doi:10.1021/ac0604235.

Crum, T. D., and R. L. Alberty (1993), The WSR-88D and the WSR-88D operational support facility, *Bull. Am. Meteorol. Soc.*, *74*(9), 1669–1687, doi:10.1175/1520-0477(1993)074<1669:TWATWO>2.0.CO;2.

Cummings, K. A. (Ed.) (2015), *A WRF-Chem Analysis of Flash Rates, Lightning-NO_x Production and Subsequent Trace Gas Chemistry of the 29–30 May 2012 Convective Event in Oklahoma During DC3*, Am. Meteorol. Soc., Phoenix, Ariz.

DeCaria, A. J., K. E. Pickering, G. L. Stenchikov, and L. E. Ott (2005), Lightning-generated NO_x and its impact on tropospheric ozone production: A three-dimensional modeling study of a Stratosphere-Troposphere Experiment: Radiation, Aerosols and Ozone (STERAO-A) thunderstorm, *J. Geophys. Res.*, *110*, D14303, doi:10.1029/2004JD005556.

Dickerson, R. R., et al. (1987), Thunderstorms: An important mechanism in the transport of air pollutants, *Science*, *235*(4787), 460–465, doi:10.1126/science.235.4787.460.

Diskin, G. S., J. R. Podolske, G. W. Sachse, and T. A. Slate (2002), Open-path airborne tunable diode laser hygrometer, *Proc. SPIE*, *4817*, 196–204, doi:10.1117/12.453736.

Emmons, L. K., et al. (2010), Description and evaluation of the Model for Ozone and Related chemical Tracers, version 4 (MOZART-4), *Geosci. Model Dev.*, *3*(1), 43–67, doi:10.5194/gmd-3-43-2010.

Facchini, M. C., et al. (1992), Phase-partitioning and chemical reactions of low molecular weight organic compounds in fog, *Tellus B*, *44*(5), 533–544, doi:10.1034/j.1600-0889.1992.t01-3-00007.x.

Fahey, K. M., and S. N. Pandis (2001), Optimizing model performance: Variable size resolution in cloud chemistry modeling, *Atmos. Environ.*, *35*(26), 4471–4478, doi:10.1016/S1352-2310(01)00224-2.

Fast, J. D., W. I. Gustafson, R. C. Easter, R. A. Zaveri, J. C. Barnard, E. G. Chapman, G. A. Grell, and S. E. Peckham (2006), Evolution of ozone, particulates, and aerosol direct radiative forcing in the vicinity of Houston using a fully coupled meteorology-chemistry-aerosol model, *J. Geophys. Res.*, *111*, D21305, doi:10.1029/2005JD006721.

Fierro, A. O., E. R. Mansell, C. L. Ziegler, and D. R. MacGorman (2012), Application of a lightning data assimilation technique in the WRF-ARW model at cloud-resolving scales for the tornado outbreak of 24 May 2011, *Mon. Weather Rev.*, *140*(8), 2609–2627, doi:10.1175/MWR-D-11-00299.1.

Fried, A., et al. (2008), Role of convection in redistributing formaldehyde to the upper troposphere over North America and the North Atlantic during the summer 2004 INTEX campaign, *J. Geophys. Res.*, *113*, D17306, doi:10.1029/2007JD009760.

Gerbig, C., S. Schmitgen, D. Kley, A. Volz-Thomas, K. Dewey, and D. Haaks (1999), An improved fast-response vacuum-UV resonance fluorescence CO instrument, *J. Geophys. Res.*, *104*(D1), 1699–1704, doi:10.1029/1998JD100031.

Grassian, V. H. (2005), *Environmental Catalysis*, CRC Press, Boca Raton, Fla.

Grell, G. A., S. E. Peckham, R. Schmitz, S. A. McKeen, G. Frost, W. C. Skamarock, and B. Eder (2005), Fully coupled "online" chemistry within the WRF model, *Atmos. Environ.*, *39*(37), 6957–6975, doi:10.1016/j.atmosenv.2005.04.027.

Guenther, A., T. Karl, P. Harley, C. Wiedinmyer, P. I. Palmer, and C. Geron (2006), Estimates of global terrestrial isoprene emissions using MEGAN (Model of Emissions of Gases and Aerosols from Nature), *Atmos. Chem. Phys.*, *6*(11), 3181–3210, doi:10.5194/acp-6-3181-2006.

Hegg, D. A., and T. V. Larson (1990), The effects of microphysical parameterization on model predictions of sulfate production in clouds, *Tellus B*, *42*(3), 272–284, doi:10.1034/j.1600-0889.1990.t01-2-00006.x.

Homeyer, C. R. (2014), Formation of the enhanced-V infrared cloud-top feature from high-resolution three-dimensional radar observations, *J. Atmos. Sci.*, *71*(1), 332–348, doi:10.1175/JAS-D-13-079.1.

Homeyer, C. R., and M. R. Kumjian (2015), Microphysical characteristics of overshooting convection from polarimetric radar observations, *J. Atmos. Sci.*, *72*(2), 870–891, doi:10.1175/JAS-D-13-0388.1.

Hong, S.-Y., Y. Noh, and J. Dudhia (2006), A new vertical diffusion package with an explicit treatment of entrainment processes, *Mon. Weather Rev.*, *134*(9), 2318–2341, doi:10.1175/MWR3199.1.

Hudman, R. C., et al. (2007), Surface and lightning sources of nitrogen oxides over the United States: Magnitudes, chemical evolution, and outflow, *J. Geophys. Res.*, *112*, D12S05, doi:10.1029/2006JD007912.

Huey, L. G. (2007), Measurement of trace atmospheric species by chemical ionization mass spectrometry: Speciation of reactive nitrogen and future directions, *Mass Spectrom. Rev.*, *26*(2), 166–184, doi:10.1002/mas.20118.

Huey, L. G., P. W. Villalta, E. J. Dunlea, D. R. Hanson, and C. J. Howard (1996), Reactions of CF_3O^- with atmospheric trace gases, *J. Phys. Chem.*, *100*(1), 190–194, doi:10.1021/jp951928u.

Iacono, M. J., J. S. Delamere, E. J. Mlawer, M. W. Shephard, S. A. Clough, and W. D. Collins (2008), Radiative forcing by long-lived greenhouse gases: Calculations with the AER radiative transfer models, *J. Geophys. Res.*, *113*, D13103, doi:10.1029/2008JD009944.

IPCC (2001), *Climate Change 2001: The Scientific Basis*, Cambridge Univ. Press, Cambridge, U. K.

Iribarne, J., and T. Pyshnov (1990), The effect of freezing on the composition of supercooled droplets—I. Retention of HCl, HNO_3, NH_3 and H_2O_2, *Atmos. Environ. Part A*, *24*(2), 383–387, doi:10.1016/0960-1686(90)90118-7.

Jacob, D. J. (1986), Chemistry of OH in remote clouds and its role in the production of formic acid and peroxymonosulfate, *J. Geophys. Res.*, *91*(D9), 9807–9826, doi:10.1029/JD091iD09p09807.

Jaeglé, L., D. J. Jacob, W. H. Brune, D. Tan, I. C. Faloona, A. J. Weinheimer, B. A. Ridley, T. L. Campos, and G. W. Sachse (1998), Sources of HO_x and production of ozone in the upper troposphere over the United States, *Geophys. Res. Lett.*, *25*(10), 1709–1712, doi:10.1029/98GL00041.

Kärcher, B., and M. M. Basko (2004), Trapping of trace gases in growing ice crystals, *J. Geophys. Res.*, *109*, D22204, doi:10.1029/2004JD005254.

Kärcher, B., and C. Voigt (2006), Formation of nitric acid/water ice particles in cirrus clouds, *Geophys. Res. Lett.*, *33*, L08806, doi:10.1029/2006GL025927.

Keene, W. C., B. W. Mosher, D. J. Jacob, J. W. Munger, R. W. Talbot, R. S. Artz, J. R. Maben, B. C. Daube, and J. N. Galloway (1995), Carboxylic acids in clouds at a high-elevation forested site in central Virginia, *J. Geophys. Res.*, *100*(D5), 9345–9357, doi:10.1029/94JD01247.

Kim, S. et al. (2007), Measurement of $HO2_NO_2$ in the free troposphere during the Intercontinental Chemical Transport Experiment–North America 2004 in the free troposphere during the Intercontinental Chemical Transport Experiment–North America 2004, *J. Geophys. Res.*, *112*, D12S01, doi:10.1029/2006JD007676.

Koren, V., J. Schaake, K. Mitchell, Q.-Y. Duan, F. Chen, and J. M. Baker (1999), A parameterization of snowpack and frozen ground intended for NCEP weather and climate models, *J. Geophys. Res.*, *104*(D16), 19,569–19,585, doi:10.1029/1999JD900232.

Korolev, A. V., E. F. Emery, J. W. Strapp, S. G. Cober, G. A. Isaac, M. Wasey, and D. Marcotte (2011), Small ice particles in tropospheric clouds: Fact or artifact? Airborne Icing Instrumentation Evaluation experiment, *Bull. Am. Meteorol. Soc.*, *92*(8), 967–973, doi:10.1175/2010BAMS3141.1.

Lance, S., C. A. Brock, D. Rogers, and J. A. Gordon (2010), Water droplet calibration of the Cloud Droplet Probe (CDP) and in-flight performance in liquid, ice and mixed-phase clouds during ARCPAC, *Atmos. Meas. Tech.*, *3*(6), 1683–1706, doi:10.5194/amt-3-1683-2010.

Lebo, Z. J., and H. Morrison (2015), Effects of horizontal and vertical grid spacing on mixing in simulated squall lines and implications for convective strength and structure, *Mon. Weather Rev.*, *143*(11), 4355–4375, doi:10.1175/MWR-D-15-0154.1.

Lelieveld, J., and P. J. Crutzen (1990), Influences of cloud photochemical processes on tropospheric ozone, *Nature*, *343*(6255), 227–233.

Leriche, M., J.-P. Pinty, C. Mari, and D. Gazen (2013), A cloud chemistry module for the 3-D cloud-resolving mesoscale model Meso-NH with application to idealized cases, *Geosci. Model Dev.*, *6*(4), 1275–298, doi:10.5194/gmd-6-1275-2013.

Madronich, S. (1987), Photodissociation in the atmosphere: 1. Actinic flux and the effects of ground reflections and clouds, *J. Geophys. Res.*, *92*(D8), 9740–9752, doi:10.1029/JD092iD08p09740.

Martin, L., and T. W. Good (1991), Catalyzed oxidation of sulfur dioxide in solution: The iron-manganese synergism, *Atmos. Environ. Part A*, *25*(10), 2395–2399, doi:10.1016/0960-1686(91)90113-L.

Mecikalski, R. M., A. L. Bain, and L. D. Carey (2015), Radar and lightning observations of deep moist convection across northern Alabama during DC3: 21 May 2012, *Mon. Weather Rev.*, *143*, 2774–2794, doi:10.1175/MWR-D-14-00250.1.

Morrison, H., G. Thompson, and V. Tatarskii (2009), Impact of cloud microphysics on the development of trailing stratiform precipitation in a simulated squall line: Comparison of one- and two-moment schemes, *Mon. Weather Rev.*, *137*(3), 991–1007, doi:10.1175/2008MWR2556.1.

Munger, J. W., D. J. Jacob, B. C. Daube, L. W. Horowitz, W. C. Keene, and B. G. Heikes (1995), Formaldehyde, glyoxal, and methylglyoxal in air and cloudwater at a rural mountain site in central Virginia, *J. Geophys. Res.*, *100*(D5), 9325–9333, doi:10.1029/95JD00508.

Neu, J. L., and M. J. Prather (2012), Toward a more physical representation of precipitation scavenging in global chemistry models: Cloud overlap and ice physics and their impact on tropospheric ozone, *Atmos. Chem. Phys.*, *12*(7), 3289–3310, doi:10.5194/acp-12-3289-2012.

Pandis, S. N., and J. H. Seinfeld (1989), Sensitivity analysis of a chemical mechanism for aqueous-phase atmospheric chemistry, *J. Geophys. Res.*, *94*(D1), 1105–1126, doi:10.1029/JD094iD01p01105.

Prather, M. J., and D. J. Jacob (1997), A persistent imbalance in HO_x and NO_x photochemistry of the upper troposphere driven by deep tropical convection, *Geophys. Res. Lett.*, *24*(24), 3189–3192, doi:10.1029/97GL03027.

Price, C., and D. Rind (1992), A simple lightning parameterization for calculating global lightning distributions, *J. Geophys. Res.*, *97*(D9), 9919–9933, doi:10.1029/92JD00719.

Pruppacher, H. R., and J. Klett (1997), *Microphysics of Clouds and Precipitation*, Kluwer Acad., Norwell, Mass.

Richter, D., P. Weibring, J. Walega, A. Fried, S. Spuler, and M. Taubman (2015), Compact highly sensitive multi-species airborne mid-IR spectrometer, *Appl. Phys. B*, *119*(1), 119–131, doi:10.1007/s00340-015-6038-8.

Ridley, B. A., and F. E. Grahek (1990), A small, low flow, high sensitivity reaction vessel for NO chemiluminescence detectors, *J. Atmos. Oceanic Technol.*, *7*(2), 307–311, doi:10.1175/1520-0426(1990)007<0307:ASLFHS>2.0.CO;2.

Ridley, B. A., F. E. Grahek, and J. G. Walega (1992), A small high-sensitivity, medium-response ozone detector suitable for measurements from light aircraft, *J. Atmos. Oceanic Technol.*, *9*(2), 142–148, doi:10.1175/1520-0426(1992)009<0142:ASHSMR>2.0.CO;2.

Roelofs, G. (1993), A cloud chemistry sensitivity study and comparison of explicit and bulk cloud model performance, *Atmos. Environ. Part A*, *27*(15), 2255–2264, doi:10.1016/0960-1686(93)90396-G.

Ryerson, T. B., E. J. Williams, and F. C. Fehsenfeld (2000), An efficient photolysis system for fast-response NO_2 measurements, *J. Geophys. Res.*, *105*(D21), 26,447–26,461, doi:10.1029/2000JD900389.

Sachse, G. W., G. F. Hill, L. O. Wade, and M. G. Perry (1987), Fast-response, high-precision carbon monoxide sensor using a tunable diode laser absorption technique, *J. Geophys. Res.*, *92*(D2), 2071–2081, doi:10.1029/JD092iD02p02071.

Schwartz, S. (1986), Mass-Transport Considerations Pertinent to Aqueous Phase Reactions of Gases in Liquid-Water Clouds, in *Chemistry of Multiphase Atmospheric Systems, NATO ASI Ser.*, vol. 6, edited by W. Jaeschke, pp. 415–471, Springer, Berlin, doi:10.1007/978-3-642-70627-1_16.

Seinfeld, J., and S. Pandis (2006), *Atmospheric Chemistry and Physics: From Air Pollution to Climate Change*, Wiley, New York.

Snider, J. R., and J. Huang (1998), Factors influencing the retention of hydrogen peroxide and molecular oxygen in rime ice, *J. Geophys. Res.*, *103*(D1), 1405–1415, doi:10.1029/97JD02847.

Snider, J. R., D. C. Montague, and G. Vali (1992), Hydrogen peroxide retention in rime ice, *J. Geophys. Res.*, *97*(D7), 7569–7578, doi:10.1029/92JD00237.

Snow, J. A., B. G. Heikes, H. Shen, D. W. O'Sullivan, A. Fried, and J. Walega (2007), Hydrogen peroxide, methyl hydroperoxide, and formaldehyde over North America and the North Atlantic, *J. Geophys. Res.*, *112*, D12S07, doi:10.1029/2006JD007746.

St. Clair, J. M., D. C. McCabe, J. D. Crounse, U. Steiner, and P. O. Wennberg (2010), Chemical ionization tandem mass spectrometer for the in situ measurement of methyl hydrogen peroxide, *Rev. Sci. Instrum.*, *81*(9), 094102, doi:10.1063/1.3480552.

Stickler, A., H. Fischer, J. Williams, M. de Reus, R. Sander, M. G. Lawrence, J. N. Crowley, and J. Lelieveld (2006), Influence of summertime deep convection on formaldehyde in the middle and upper troposphere over Europe, *J. Geophys. Res.*, *111*, D14308, doi:10.1029/2005JD007001.

Stuart, A. L., and M. Z. Jacobson (2004), Chemical retention during dry growth riming, *J. Geophys. Res.*, *109*, D07305, doi:10.1029/2003JD004197.

Tabazadeh, A., O. B. Toon, and E. J. Jensen (1999), A surface chemistry model for nonreactive trace gas adsorption on ice: Implications for nitric acid scavenging by cirrus, *Geophys. Res. Lett.*, *26*(14), 2211–2214, doi:10.1029/1999GL900501.

Ullerstam, M., and J. P. D. Abbatt (2005), Burial of gas-phase HNO_3 by growing ice surfaces under tropospheric conditions, *Phys. Chem. Chem. Phys.*, *7*, 3596–3600, doi:10.1039/B507797D.

Voigt, C., H. Schlager, H. Ziereis, B. Kärcher, B. P. Luo, C. Schiller, M. Krämer, P. J. Popp, H. Irie, and Y. Kondo (2006), Nitric acid in cirrus clouds, *Geophys. Res. Lett.*, *33*, L05803, doi:10.1029/2005GL025159.

Voisin, D., M. Legrand, and N. Chaumerliac (2000), Scavenging of acidic gases (HCOOH, CH_3COOH, HNO_3, HCl, and SO_2) and ammonia in mixed liquid-solid water clouds at the Puy de Dôme mountain (France), *J. Geophys. Res.*, *105*(D5), 6817–6835, doi:10.1029/1999JD900983.

von Blohn, N., K. Diehl, S. K. Mitra, and S. Borrmann (2011), Wind tunnel experiments on the retention of trace gases during riming: Nitric acid, hydrochloric acid, and hydrogen peroxide, *Atmos. Chem. Phys.*, *11*(22), 11,569–11,579, doi:10.5194/acp-11-11569-2011.

Walcek, C. J., and G. R. Taylor (1986), A theoretical method for computing vertical distributions of acidity and sulfate production within cumulus clouds, *J. Atmos. Sci.*, *43*(4), 339–355, doi:10.1175/1520-0469(1986)043<0339:ATMFCV>2.0.CO;2.

Weibring, P., D. Richter, A. Fried, J. Walega, and C. Dyroff (2006), Ultra-high-precision mid-IR spectrometer. II: System description and spectroscopic performance, *Appl. Phys. B*, *85*(2–3), 207–218, doi:10.1007/s00340-006-2300-4.

Weibring, P., D. Richter, J. G. Walega, and A. Fried (2007), First demonstration of a high performance difference frequency spectrometer on airborne platforms, *Opt. Express*, *15*(21), 13,476–13,495, doi:10.1364/OE.15.013476.

Wiedinmyer, C., S. K. Akagi, R. J. Yokelson, L. K. Emmons, J. A. Al-Saadi, J. J. Orlando, and A. J. Soja (2011), The Fire INventory from NCAR (FINN): A high resolution global model to estimate the emissions from open burning, *Geosci. Model Dev.*, *4*(3), 625–641, doi:10.5194/gmd-4-625-2011.

Yang, Q., et al. (2015), Aerosol transport and wet scavenging in deep convective clouds: A case study and model evaluation using a multiple passive tracer analysis approach, *J. Geophys. Res. Atmos.*, *120*, 8448–8468, doi:10.1002/2015JD023647.

Zaveri, R. A., R. C. Easter, J. D. Fast, and L. K. Peters (2008), Model for Simulating Aerosol Interactions and Chemistry (MOSAIC), *J. Geophys. Res.*, *113*, D13204, doi:10.1029/2007JD008782.

Zhang, J., W. Gong, W. R. Leaitch, and J. W. Strapp (2007), Evaluation of modeled cloud properties against aircraft observations for air quality applications, *J. Geophys. Res.*, *112*, D10S16, doi:10.1029/2006JD007596.

Zondlo, M. A., S. B. Barone, and M. A. Tolbert (1997), Uptake of HNO_3 on ice under upper tropospheric conditions, *Geophys. Res. Lett.*, *24*(11), 1391–1394, doi:10.1029/97GL01287.

Zondlo, M. A., M. E. Paige, S. M. Massick, and J. A. Silver (2010), Vertical cavity laser hygrometer for the National Science Foundation Gulfstream-V aircraft, *J. Geophys. Res.*, *115*, D20309, doi:10.1029/2010JD014445.